



Lawrence Berkeley National Laboratory

Efficient modeling of optically-complex, non-coplanar exterior shading: Validation of matrix algebraic methods

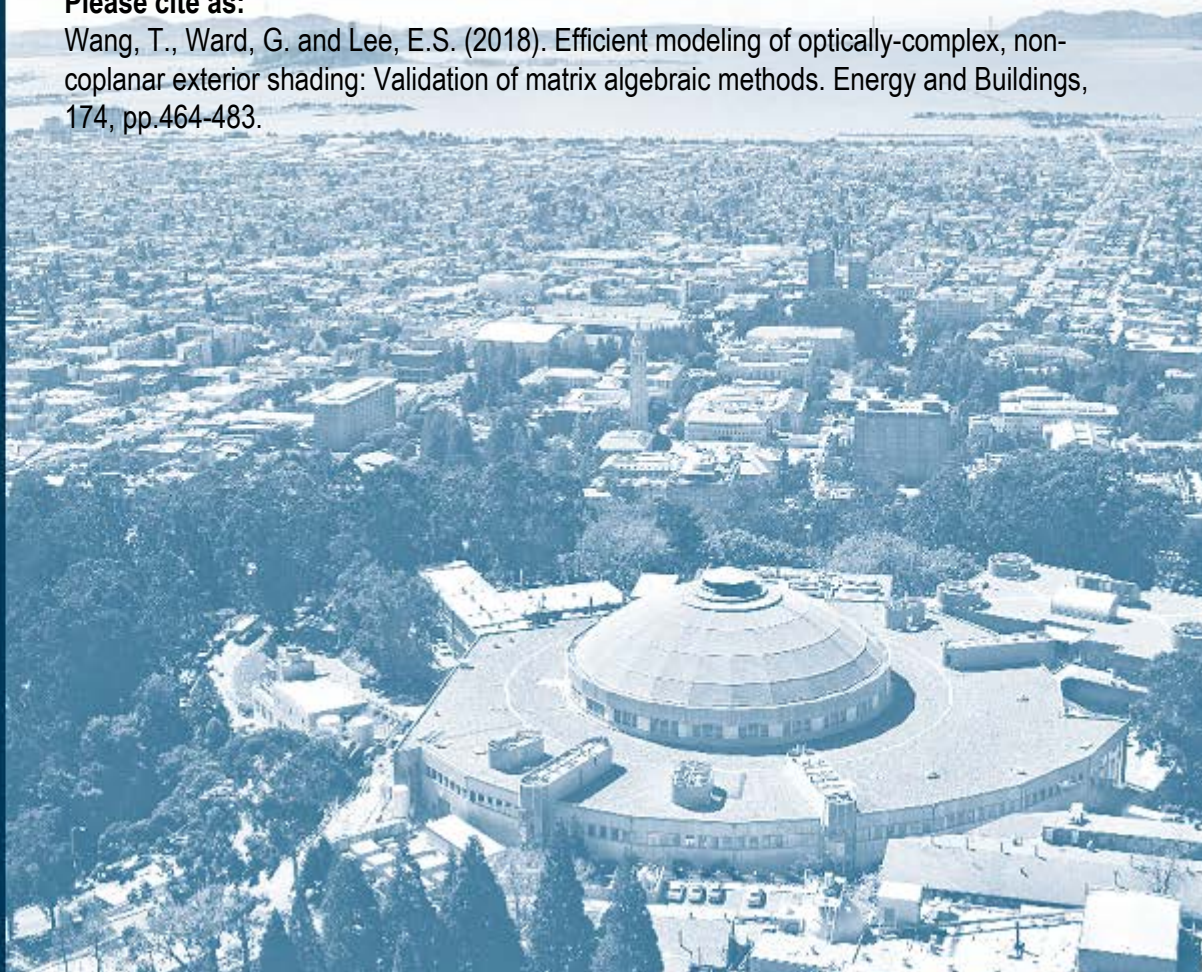
Taoning Wang^a
Gregory Ward^b
Eleanor S. Lee^a

Lawrence Berkeley National Laboratory^a
Anywhere Software^b

Energy Technologies Area
September 2018

Please cite as:

Wang, T., Ward, G. and Lee, E.S. (2018). Efficient modeling of optically-complex, non-coplanar exterior shading: Validation of matrix algebraic methods. *Energy and Buildings*, 174, pp.464-483.



Disclaimer:

This document was prepared as an account of work sponsored by the United States Government. While this document is believed to contain correct information, neither the United States Government nor any agency thereof, nor the Regents of the University of California, nor any of their employees, makes any warranty, express or implied, or assumes any legal responsibility for the accuracy, completeness, or usefulness of any information, apparatus, product, or process disclosed, or represents that its use would not infringe privately owned rights. Reference herein to any specific commercial product, process, or service by its trade name, trademark, manufacturer, or otherwise, does not necessarily constitute or imply its endorsement, recommendation, or favoring by the United States Government or any agency thereof, or the Regents of the University of California. The views and opinions of authors expressed herein do not necessarily state or reflect those of the United States Government or any agency thereof or the Regents of the University of California.

Efficient modeling of optically-complex, non-coplanar exterior shading: Validation of matrix algebraic methods

Taoning Wang^a, Gregory Ward^b, Eleanor S. Lee^a

^a *Building Technologies and Urban Systems Division, Energy Technologies Area, Lawrence Berkeley National Laboratory, Mailstop 90-3111, 1 Cyclotron Road, Berkeley, California 94720 USA*

^b *Anywhere Software, 950 Creston Road, Berkeley, California, 94708 USA*

Abstract

It has long been established that shading windows with overhangs, fins, and other types of non-coplanar systems (NCS) is one of the most effective ways of controlling solar heat gains in buildings because they intercept solar radiation prior to entry into the building. Designers however often specify non-opaque materials (e.g., louvers, fritted glass, expanded metal mesh) for these systems in order to admit daylight, reduce lighting energy use, and improve indoor environmental quality. Most simulation tools rely on geometric calculations and radiosity methods to model the solar heat gain impacts of NCS and cannot model optically-complex materials or geometries. For daylighting analysis, optically-complex NCS can be modeled using matrix algebraic methods, although time-efficient parametric analysis has not yet been implemented. Determining the best design and/or material for static or operable NCS that minimize cooling, heating, and lighting energy use and peak demand requires an iterative process. This study describes and validates a matrix algebraic method that enables parametric energy analysis of NCS. Such capabilities would be useful not only for design but also for development of prescriptive energy-efficiency standards, rating and labeling systems for commercial products, development of design guidelines, and development of more optimal NCS technologies.

A facade or “F” matrix, which maps the transfer of flux from the NCS to the surface of the window, is introduced and its use is explained. A field study was conducted in a full-scale outdoor testbed to measure the daylight performance of an operable drop-arm awning. Simulated data were compared to measured data in order to validate the models. Results demonstrated model accuracy: simulated workplane illuminance was within 11-13%, surface luminance was within 16-18%, and the daylight glare probability was within 6-9% of measured results. Methods used to achieve accurate results are discussed. Results of the validation of daylighting performance are applicable to solar heat gain performance. Since exterior shading can also significantly reduce peak demand, these models enable stakeholders to more accurately assess HVAC and lighting impacts in support of grid management and resiliency goals.

Keywords: exterior shading; daylighting; solar heat gains; bidirectional scattering distribution function (BSDF); validation; building energy simulation tools; windows.

1. Introduction

Annual primary energy use in buildings was 41 EJ or 39 quadrillion Btu (39×10^{15} Btu) in the United States in 2010 and is projected to increase to 47 EJ (45 quad) by 2035. The residential sector accounts for 54% of total building energy use while the commercial sector accounts for the remaining 46%. Of the total aggregate load for both sectors, 0.797 EJ (0.756 quad) of cooling load is attributable to solar heat gains through windows. These same solar gains offset the need for heating by 0.574 EJ (0.544 quad) and have the potential to reduce lighting energy use in the commercial sector by 1.06 EJ (1 quad) through daylighting [1-4].

Prior studies have quantified the solar control benefit of exterior (outdoor) coplanar and non-coplanar shading (NCS) systems on reducing energy use and peak demand [5-11]. These systems intercept solar radiation prior to entry into the building and can thus be more effective than between-pane and interior (indoor) shading systems. Poorly designed solar control technologies however can decrease cooling load at the expense of increased heating load and lighting energy use. Industry has an intuitive understanding of these tradeoffs between solar control and daylighting (e.g., blocking sunlight reduces daylight). This is evidenced both with commercially available products and design practice: use of opaque shading elements with no transmissive properties is less typical; awnings, canopies, and architectural solutions are more often specified with fabrics, louvers, perforated metal, expanded metal mesh, fritted glass, and other materials to partially block direct sunlight and allow filtered daylight to come through. Operable shading such as drop arm awnings or adjustable louvers provide further opportunities to reduce energy use and peak demand through daily or seasonal adjustments in order to minimize both heating and cooling loads.

Historically, simulation tools have used geometrical calculations and/or radiosity methods to quantify the effect of NCS on window heat gains and daylighting [12-17]. Kiritat et al. [18] provided a detailed comprehensive review of simulation modeling tools for shading systems. The key drawback of these tools is that the underlying method excludes many of the optically-complex materials that are specified for exterior shading (e.g., fritted glass, perforated metal, etc.). With the introduction of matrix algebraic models, such as the two-, three-, and five-phase methods [19-27], simulation tools have been able to employ time-efficient ray-tracing methods to determine annual energy performance of optically-complex shading and daylighting systems at a fraction of the time needed for full ray-tracing calculations.

The sole limitation of these methods is that the matrix used to map flux from the discretized sky to the surface of the window (called the daylight or “D” matrix) includes both the NCS and exterior obstructions, such as mountains or nearby buildings. This prevents parametric analysis of the NCS element in isolation from the other obstructions. Analysis of a few NCS designs (or in the case of an operable NCS with a few discrete positions) can be accomplished by computing a D matrix for each permutation of the NCS design. For most architects and engineers, this can be achieved routinely using the existing matrix-based simulation tools today. Applications involving hundreds or thousands of permutations of the NCS design and surrounding environment (e.g., window orientation, nearby obstructions, etc.) however would need an alternate approach. Such applications include development of prescriptive energy-efficiency standards to promote more optimal exterior shading. Rating and labeling of commercially available shading systems could be more easily accomplished by organizations such as the US Attachments Energy Rating Council [28] and the European Solar-Shading Organization [29]. Parametric analysis could also be applied to the development of new solar control/ daylight-redirecting NCS technologies or to develop design guidance for existing shading systems offered by manufacturers [30-33].

In this study, we describe alternate modeling approaches, called the four- and six-phase methods, that were developed to separate the flux transfer behavior of the NCS from the D matrix, enabling parametric analysis. This was accomplished with the introduction of a new facade or “F” matrix.¹ This study describes methods to construct the F matrix, then compares measured data from a full-scale outdoor testbed facility to simulations in order to validate the methods. Validation of new models is an important step toward adoption in commercial software tools. Validation provides an opportunity to examine deficiencies in the model, improve the underlying algorithms, understand the limitations of the model, and increase confidence in the use of the models for real world building applications. Results of the validation are provided. Implications of the new methods are discussed.

2. Background

The methods described in this paper use *Radiance* as the simulation engine. Radiance is a suite of tools that perform backward ray tracing and other calculations to model and render the luminous effects of fenestration and lighting systems [33]. Radiance can simulate the flux transfer of a non-coplanar shading (NCS) element using ray tracing methods. However, conventional ray tracing can take a considerable amount of time to model a single point-in-time daylight condition. In order to reduce computation time for an annual calculation, the concept of the daylight coefficient was introduced in 1983 [19], which laid out the mathematical function that relates the luminance of the sky to the illuminance of a point in a room. The concept was later realized and improved upon with the introduction of the Radiance *rcontrib* tool [34-35]. The original daylight coefficient method (also called the two-phase method) enabled efficient daylight calculations with a discretized sky luminance distribution. The three- and five-phase methods were developed later to allow parametric analysis of coplanar complex fenestration systems using bidirectional scattering distribution function (BSDF) data and enable more accurate prediction of the distribution of direct sunlight in the space [25, 27]. Before the introduction of the Radiance *rfluxmtx* tool [35], users could only model coplanar, rectangular fenestration systems such as one with a double-glazed window and a venetian blind. The Radiance *rfluxmtx* tool enabled the flux transfer calculation between two non-parallel, non-rectangular surfaces, which in turn enabled the development of the four- and six-phase methods to facilitate evaluation of non-coplanar shading systems.

2.1. Modeling NCS using existing methods

There are several existing methods that can be used to simulate the daylighting performance of a NCS. The full ray tracing calculation using the Radiance *rtrace* tool is the most accurate “ground truth” approach. The Radiance two-, three-, and five-phase methods can be used to evaluate the performance of a NCS, but these methods incorporate the NCS element as a fixed part of the scene. The performance of the NCS cannot be separated and stored in a matrix to be used for example in a parametric design analysis of different glass frit patterns for an overhang or to model an operable awning.

The matrix algebraic modeling approaches are explained as follows: To derive a flux transfer matrix, there are two key components: senders and receivers. A sender is a surface with a direction that randomly sends out rays in a hemisphere. The rays interact with the objects in the scene before arriving at one or more receivers. The receivers then sort rays into bins based on the specified sampling basis. Thus, the flux transfer between a sender and a receiver is stored in a matrix with the dimension of (number of sender directions \times number of receiver bins). Multiple matrices may be produced in a single run in the case of multiple receivers.

¹ Andrew McNeil (previously at LBNL) was the originator of the F-matrix concept.

2.1.1. Two-phase method

The two-phase or daylight coefficient (DC) method can be used to calculate the annual daylighting performance of an NCS. With the two-phase method, the sky dome hemisphere is subdivided into a grid of solid angles or “patches,” then the relationship between the luminance of each sky patch and the illuminance or luminance of a point in space is calculated and stored in a matrix format. In this case, the sensor point in the room is the sender and the sky dome is the receiver. Given a sky luminance distribution, the illuminance at the point in a room can be calculated by multiplying the luminance of each sky patch by the corresponding coefficient in the matrix and summing for all sky patches. The accuracy of the result increases with increased sky subdivisions. With the two-phase method, the NCS will be placed in the scene and be part of the ray tracing from the indoor sensor point to the sky. The daylight coefficient matrix needs to be re-computed when any part of the scene changes.

$$\mathbf{E} = \mathbf{V}^* \mathbf{S} \quad (1)$$

where,

- \mathbf{E} is the resulting illuminance or irradiance value (or luminance, L);
- \mathbf{S} is the sky matrix, representing the luminance distribution of the discretized skydome hemisphere for the year;
- \mathbf{V}^* is the view matrix that stores the flux transfer between the indoor sensor point (sender) and the sky (receiver).

2.1.2. Three-phase method

With the two-phase method, the number of simulations increases exponentially with the number of changing elements in a scene. With the three-phase method, the ray-tracing path is separated at the fenestration system. Rays are no longer traced from the indoor sensor point to the sky. Instead, rays are traced from the sensor point to the window surface, and then from the window surface to the sky. In this way, the indoor and outdoor flux transfers are stored in two separate matrices. The flux transfer behavior of a complex fenestration system is also stored in a separate matrix. With the three-phase method, changes in the scene may require re-computing only one of the three corresponding matrices, instead of re-computing the entire two-phase matrix that was calculated by tracing from the indoor sensor to the sky. The resultant illuminance (or luminance) is obtained through matrix multiplication:

$$\mathbf{E} = \mathbf{V} \mathbf{T} \mathbf{D} \mathbf{S} \quad (2)$$

where,

- \mathbf{E} is the resulting illuminance or irradiance value (or luminance, L);
- \mathbf{S} is the sky matrix, representing the luminance distribution of the discretized skydome hemisphere for the year;
- \mathbf{D} is the daylight matrix that stores the flux transfer between the window (sender) and the sky (receiver);
- \mathbf{T} is the transmission matrix that relates the incident and exiting direction of the fenestration system (e.g., venetian blind); and,
- \mathbf{V} is the view matrix that represents the light transported from the indoor sensor point (sender) to the window (receiver).

Multiplying the V, T, and D matrices results in the daylight coefficient two-phase matrix. To model the NCS with the three-phase method, the NCS needs to be modeled as part of the daylight matrix, and changing the configuration of a NCS requires re-computing the daylight (D) matrix. This is an inefficient approach if the rest of the outdoor space remains unchanged.

2.1.3. Five-phase method

The five-phase method was introduced to improve modeling of the direct sun component [27, 36]. With the two- and three-phase methods, the solar disc is represented by the three to four sky patches that are closest to the solar position (Figure 1, left image). Consequently, the solid angle of the sun increases from 0.5° to roughly 10° . Although the total energy emitted from the sun remains the same, the intensity decreases significantly with the increase in solid angle.

With the five-phase method, only the indirect component of the three-phase result is retained with a relatively low resolution basis (first two terms in Equations 3-4) and the result is supplemented by the direct sun component with the sun represented with a 0.5° solid angle (third term in Equations 3-4; Figure 1, right image). The formula for the five-phase method is:

$$\mathbf{E} = \mathbf{V} \mathbf{T} \mathbf{D} \mathbf{S} - \mathbf{V}_d \mathbf{T} \mathbf{D}_d \mathbf{S}_d + \mathbf{C}_{ds} \mathbf{S}_{sun} \quad (3)$$

$$\mathbf{L} = \mathbf{V} \mathbf{T} \mathbf{D} \mathbf{S} - \mathbf{V}_d \mathbf{T} \mathbf{D}_d \mathbf{S}_d + (\mathbf{C}_{R-ds} + \mathbf{C}_{F-ds}) \mathbf{S}_{sun} \quad (4)$$

where,

- \mathbf{E} and \mathbf{L} are the resulting illuminance or luminance values for the modeled period (year);
- \mathbf{S} , \mathbf{T} , \mathbf{D} , and \mathbf{V} are as described for Equation 2;
- \mathbf{V}_d , \mathbf{D}_d , and \mathbf{S}_d represent the direct-only matrices in the three-phase method;
- \mathbf{C}_{ds} or \mathbf{C}_{R-ds} (\mathbf{C}_{ds} and \mathbf{C}_{R-ds} are identical matrices) is the coefficient matrix relating the flux transfer from the sun orb for a grid of positions in the skydome hemisphere to a specified location in the interior without interreflections; the variable resolution, tensor tree BSDF of the fenestration system (with or without proxy geometry) is included in the calculation of this matrix;
- \mathbf{C}_{F-ds} is the façade-side coefficient matrix relating the flux transfer from the sun orb for a grid of positions in the skydome hemisphere to the luminance as seen at the façade itself without interreflections from the outdoors or indoors but inclusive of the contributions of direct sun on and interreflected within the fenestration system itself; variable BSDF data or the geometry of the system is also included in this calculation; and,
- \mathbf{S}_{sun} is the sky luminance distribution with only the sun luminance.

Modeling NCS is similar to the approach used in the three-phase method; the direct and indirect optical behavior of the NCS is calculated along with other fixed obstructions (e.g., nearby building wing, surrounding buildings, mountains, etc.) in the daylight (D) matrix. In summary, the two-, three-, and five-phase methods can be used to simulate annual daylighting performance of a NCS system but changing the NCS requires re-computing matrices, which can be inefficient when other elements of the scene remain unchanged.

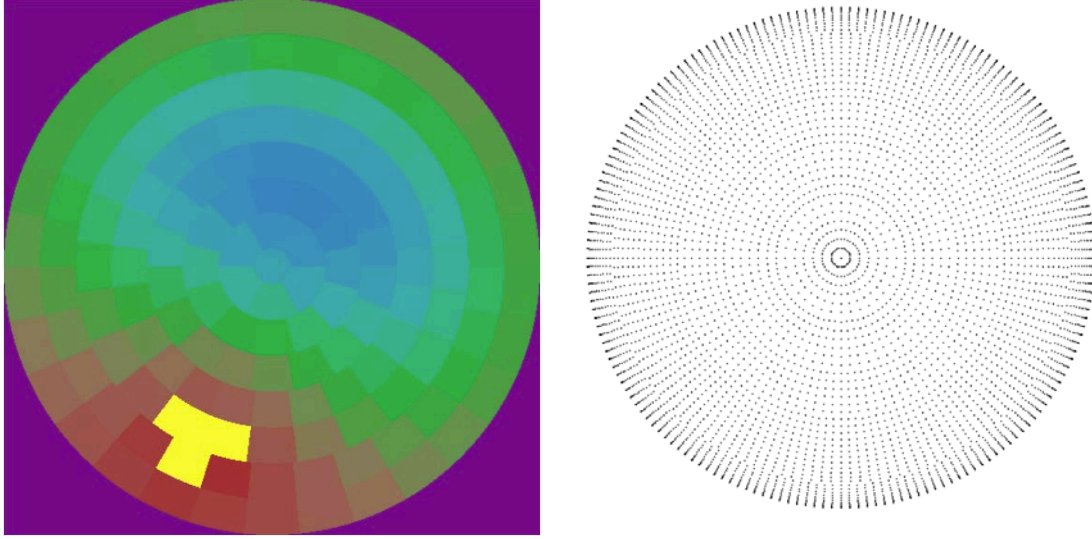


Figure 1. Sky resolution of Tregenza sky (145 basis resolution) with the sun represented by three patches in yellow (left) and 0.5° solar disc representation with the five-phase method at 5185 locations for both the Northern and Southern Hemispheres (right).

2.2. Four-phase and six-phase methods

The four-phase method is based on the three-phase method, but divides the light transported between the sky and the indoor sensor points further into four separate matrices. The newly added “facade” (F) matrix sits in between the transmission and now modified daylight matrix and captures the flux transfer between the outdoor window surface (sender) and the finite plane(s) defining the edges of the NCS (receiver) furthest from the window. Thus, the new matrix function becomes:

$$\mathbf{E} = \mathbf{V} \mathbf{T} \mathbf{F} \mathbf{D}' \mathbf{S} \quad (5)$$

The calculation of the view and transmission matrices remains unchanged from the three-phase method. Because of the added facade matrix, the daylight (D') matrix will now only include the flux transfer from the sky to the facade aperture. In addition to the benefits from the three-phase method, the four-phase method enables quick computation and comparison of various NCS configurations. The property of a NCS, such as material and geometry, can be changed and the model’s daylighting performance can be reevaluated without re-computing the other three matrices. In a similar manner, operable NCS can be modeled more efficiently.

The six-phase method naturally follows the logic from the three-phase to the five-phase method. The difference between the five- and six-phase methods is only in the indirect calculation. With the added facade matrix (F), the six-phase method formula becomes:

$$\mathbf{E} = \mathbf{V} \mathbf{T} \mathbf{F} \mathbf{D}' \mathbf{S} - \mathbf{V}_d \mathbf{T} \mathbf{F}_d \mathbf{D}'_d \mathbf{S}_d + \mathbf{C}_{ds} \mathbf{S}_{sun} \quad (6)$$

$$\mathbf{L} = \mathbf{V} \mathbf{T} \mathbf{F} \mathbf{D}' \mathbf{S} - \mathbf{V}_d \mathbf{T} \mathbf{F}_d \mathbf{D}'_d \mathbf{S}_{ds} + (\mathbf{C}_{R-ds} + \mathbf{C}_{F-ds}) \mathbf{S}_{sun} \quad (7)$$

where,

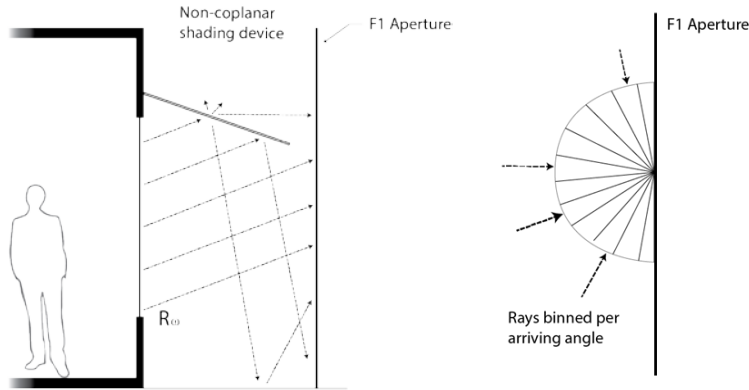


Figure 2. Left: Sampling rays are traced from the window surface to the F aperture (F matrix), as depicted by vectors R_w representing one of the outgoing directions from the defined sampling basis. These rays interact with NCP shading device (e.g., fabric awning) before arriving at the F1 aperture. Right: The rays are then binned based on their arriving angle of incidence.

- F and F_d terms represent the facade matrix and facade matrix with the direct component only, and
- D' and D'_d represents the modified daylight matrix which maps the flux transfer between the facade aperture and the sky.

Images for discomfort glare analysis can also be generated using a similar approach where Radiance computes luminance/radiance coefficients instead of illuminance/irradiance coefficients for the view matrix. For the illuminance calculation, the per window view matrix has the dimension of number of sensor points times 145 solid angles or patches (Klems resolution). For the luminance calculation, the view matrix consists of 145 images per window, where with each image represents the luminances for the chosen view due to a particular window Klems patch.

2.3. Constructing the F matrix

The F matrix represents the flux transfer properties of the NCS. An F aperture needs to be placed in the model as a ray receiver. The window surface is the ray sender. To construct the F matrix, Monte Carlo ray tracing occurs from the window surface to the F aperture. During the ray tracing process, rays interact with the NCS before it arrives at the F aperture. The incident ray's intensity and direction are recorded and binned according to the specified hemispherical sampling basis of the F aperture. The flux transfer behavior of the NCS is then stored in the F matrix. If the configuration of the NCS (e.g., materials, geometry) changes, a new F matrix needs to be computed.

There is no standard approach to construct and place the F aperture, but the ideal scenario is to place the aperture so that the rays being sampled captures all possible ways that light will interact with the NCS in the real world. In general, there are three options for defining the F aperture.

F1 aperture. The simplest way of defining an F1 aperture is by placing a finite plane parallel to the building facade that covers the corresponding window region. Figure 2 shows a section view of the ray-tracing that occurs when computing the corresponding F1 matrix. Rays sent out from the window plane in the V1 direction interact with the NCS, facade (if rays are reflected off the NCS for example back towards the window), ground and other nearby surfaces before arriving at the F1 aperture. Note that some rays are

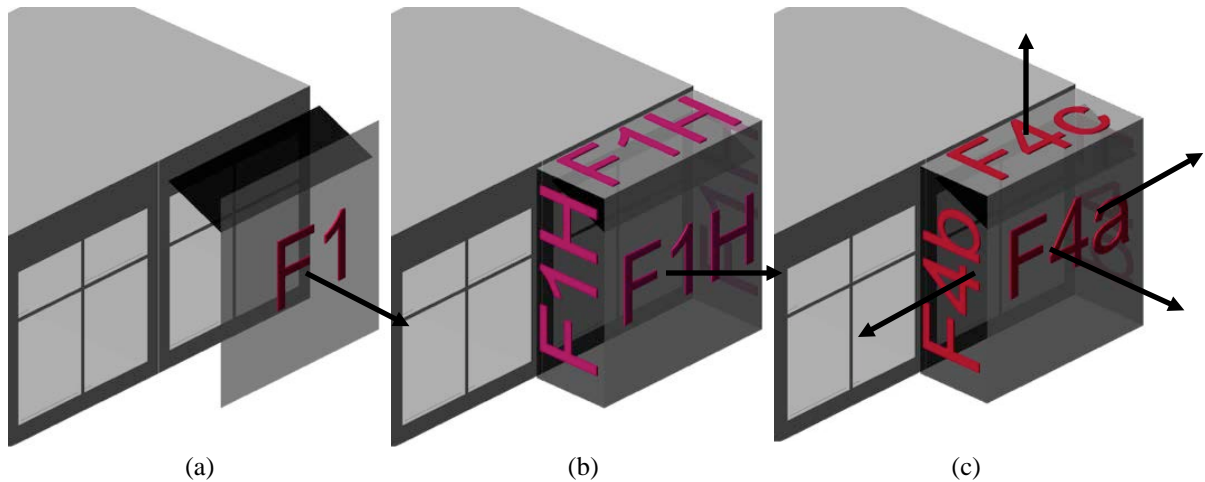


Figure 3. Construction of the F aperture. The arrows indicate the surface normal of the apertures' hemispherical sampling basis. (a) A single F aperture (F1) placed at the outer edge of the NCS; (b) a single wrapped aperture (F1H) encapsulates the NCS with a sampling direction that is slightly tilted up, resulting from averaging the four apertures' surface normal directions; (c) FN or, in this case, four F apertures encapsulate the NCS, where each aperture samples rays separately.

lost in the gap between the window and the sides of the finite-dimensioned F1 aperture, resulting in an underestimation of incident flux on the window plane. The F1 aperture samples incident rays based on the specified sampling basis (e.g., Klems 145 basis) and stores the information in the F1 matrix.

For the calculation of the modified daylight or D' matrix, rays (V2) are sent out from the F1 aperture (in the south-facing hemispherical direction for a south-facing window, for example) toward the building's surroundings. These rays interact with nearby obstructions and ground, before arriving at the subdivided skydome hemisphere. Note that direct flux from the sky dome from *behind* the F1 aperture (in the north-facing hemispherical direction) are not included in the D' matrix, again resulting in an underestimation of incident flux on the window plane. This method may be sufficient if the CFS is continuous across a long facade. An F1 aperture for an awning is shown in Figure 3(a).

F1H aperture. The F matrix can more accurately capture the NCS flux transfer if there is a continuous F1H aperture wrapping the facade. In the example shown in Figure 3 (b), the F1H aperture encapsulates the NCS with four² rectilinear planes/ polygons. Rays are traced from the window to the four receiver planes. The receiver then samples the incident rays and bins them based on a single sampling basis. The sampling basis is defined by a hemisphere whose normal (depicted by the arrow³ in Figure 3(b)) is the weighted average of the surface normals for each of the four planes/ polygons. The F1H aperture can only sample rays from a single hemispherical direction, which means that the maximum sampling angle is 180° . As a result, the F1H aperture cannot capture rays from *behind* the building facade. The FN aperture addresses this omission.

² A fifth plane with a downward facing surface normal would have been added if this example had been situated above the ground floor.

³ The arrow for the surface normal is actually pointed towards the window since the F matrix depicts the amount of flux transfer between the window and the F aperture. This, however, would have been difficult to show in the figure.

FN aperture. A more accurate way of characterizing the NCS flux transfer is to define independent F matrices for each individual F aperture then summing the flux contributions from all N F matrices. Each F aperture samples incident flux from the window source and bins the flux based on its own hemispherical basis (depicted by the surface normals in Figure 3(c)). The two F apertures that enclose the sides of the awning for this south-facing window have a hemispherical basis with a surface normal that faces east or west. For the east-facing F aperture at the end of the building, sky or ground reflected flux behind the building (from the D matrix) can now be mapped to the F matrix and the window plane. When combined, the four (or N) F matrices should capture all possible incoming flux to the window. Equation (5) extends to:

$$\mathbf{E} = \sum_{i=1}^N \mathbf{V} \mathbf{T} \mathbf{F}_i \mathbf{D} \mathbf{S} \quad (8)$$

3. Method

3.1 Description of the field test setup

Field validation of the four- and six-phase methods involved comparing simulation data to measured data in a daylit room with a non-coplanar, drop-arm fabric awning. Measurements were performed in the Lawrence Berkeley National Laboratory (LBNL) Advanced Windows Testbed (Building 71T), a full-scale instrumented testbed facility located in Berkeley, California. The test chamber was designed to emulate a typical side lit private office with a large south-facing window. The test chamber was 3.0 m (10 ft) wide by 4.6 m (15 ft) deep and 3.35 m (11 ft) high. The window consisted of double-glazed, insulated glass units (IGUs) with clear low-iron glass and Viracon VRE67 low-e coating on surface #3. The IGU had a center-of-glass visible light transmittance of 0.64, solar heat gain coefficient of 0.46 and U-value of 1.85 W/m²-K (0.33 Btu/ft²-h-°F). A horizontal mullion divided the window into a 0.76 m (2.5 ft) high upper portion and 1.7 m (5.6 ft) high lower portion. A vertical mullion divided the window in the middle. Figure 4 shows a floor plan drawing of the test chamber and photograph of the south facade with the installed awning.

The drop-arm awning was constructed with a roller shade fabric wrapped around a tubular motor that enabled the fabric to be extended out and away from the facade or retracted using a remote control interface. The awning was installed at the top of the window and spanned the full width of the window. A uniformly medium-white, linen fabric was installed (Sunbrella 4633-0000, T_{sol}=0.14, R_{sol}=0.52, T_{vis}=0.06, openness factor (OF)=0). The bidirectional scattering distribution function (BSDF) of this fabric was derived from direct and diffuse transmittance and reflectance measurements at nine angles of incidence. These measurements were performed at LBNL using a Lambda 950 spectrophotometer with a 150-mm integrating sphere and an angle tube accessory [37]. The BSDF data were represented with a Klems basis (145x145 resolution) and exhibited Lambertian diffusion. During the field test, the awning was positioned to two angles: a) 50° angle between the vertical face of the facade and the drop arm hardware used to position the awning – this awning position was enough to block most of the direct sun during the summer solstice period, and b) 125° with the awning extending all the way down during the equinox and winter solstice period, which blocked most of the view out of the window (Table 1).

Table 1

Awning test conditions and corresponding sky conditions.

Awning drop arm angle (b°)	Awning fabric angle (a°)	Test dates	Total test days	Sky conditions		
				Sunny	Overcast	Dynamic
50°	60°	July 4–30, 2016	26	12	8	6
125°	25°	November 10–18, 2016, April 25–30, 2017	14	12	2	0

Note: Angle “a” is the angle between the vertical face of the façade and the awning fabric; angle “b” is the angle between the vertical façade and the drop arm awning hardware ($b=0^\circ$ indicates the awning is fully retracted).

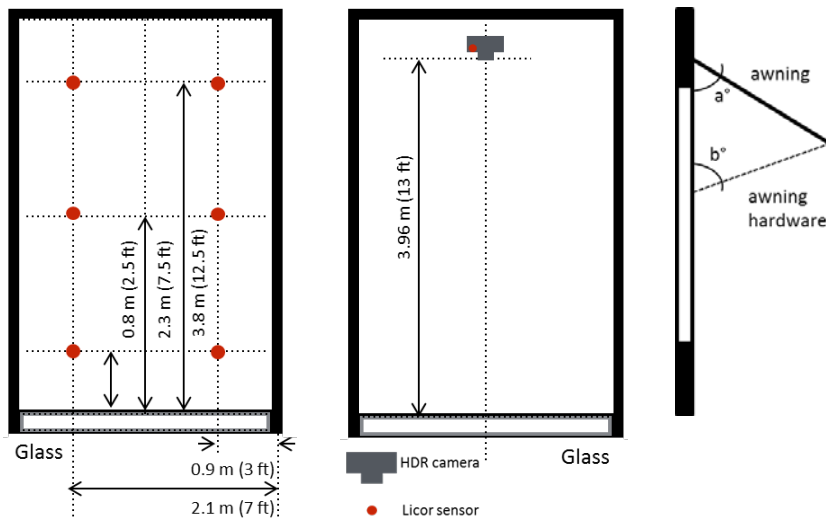


Figure 4. Top: Photograph of the facade with the awning hardware positioned at angle $b=50^\circ$; lower left: floor plan showing location of workplane illuminance sensors; lower middle: location of HDR camera with vertical illuminance sensors; lower right: vertical section showing convention for awning angles.

A high dynamic range (HDR) imaging system (Skycam, Terrestrial Light [38]) was used to measure the luminous intensity and distribution of the sky dome at 5-min intervals (see Section 3.2.1 for further information on use). Indoor conditions were recorded every 1 min using vertical and horizontal workplane illuminance sensors (LI-COR 210SA, $\pm 1.5\%$ to 7500 lux) located 1.2 m (4 ft) and 0.76 m (2.5 ft) above the floor, respectively. Figure 4 shows the locations of these sensors. HDR cameras (Canon 5D, Sigma 8mm fisheye lens) were also located in the room to measure surface luminance and discomfort glare. Image capture was automated, where measurements were taken every 5 min during daytime hours, then processed using *evalglare* [39] to produce field-of-view luminance data and daylight glare probability (DGP) values. The images were calibrated using the vertical illuminance sensors, which were positioned immediately adjacent to the center of the fisheye lens at the 1.2 m (4 ft) height. Each image was captured at 5760×3840 pixel resolution and then down-sampled to 800×800 pixels for luminance and discomfort glare analysis.

Data were collected continuously during July 2016 for the summer test condition and during mid-November 2016 and end of April 2017 for the winter solstice and equinox conditions. The climate in Berkeley during the summer and autumn periods is typically dry and sunny with frequent morning fog persisting until about 10:00 AM or noon. Winter and spring sky conditions have dynamic/ partly cloudy or clear sky conditions. Test dates and sky conditions during the tests are denoted in Table 1. A hill to the east blocked morning sun until 6:00-8:00 AM Standard Time (ST), varying by season. Simulations were modeled without the hills so measured data for the 6:00-8:00 AM ST period were excluded from the error calculations.

3.2. Description of the Radiance simulations

A Radiance model of the test space including the furniture was used for the simulations. The exterior model included a local ground plane. The exterior ground was modeled as uniformly diffusing with a visible reflectance of 0.12. The matrices were generated using the Radiance *rfluxmtx* tool, which serves as an interface for the Radiance *rcontrib* tool.⁴ The following sections describe how the matrices were generated.

3.2.1. Generation of the S matrix

The outdoor HDR sky imaging system and associated scripts from the vendor were used to produce the S matrix for the Radiance simulations of indoor illuminance and luminance. Global horizontal illuminance measurements were taken next to and within the same plane as the HDR sky imaging sensor. Diffuse horizontal illuminance was derived from the HDR image by masking out the circumsolar area. The direct normal illuminance (contribution from the sun) was calculated from the measured global horizontal illuminance and derived diffuse horizontal illuminance. The S matrix was then generated using the HDR sky luminance distribution and the derived direct normal illuminance and diffuse horizontal illuminance of the sun and sky. The Tregenza 145 hemispherical basis subdivided by a multiplication factor (MF) of four (Reinhart MF:4 sky of 2305 patches) was used to subdivide the sky into a series of solid angles or patches (Figure 5). Ground plane reflectance was used with the Perez sky model to derive ground plane luminance – this value was also included in the S matrix.

⁴ Descriptions of the *rfluxmtx* and *rcontrib* tools can be found in Radiance manual repository at: <https://radiance-online.org/learning/documentation/manual-pages>, accessed January 10, 2018.

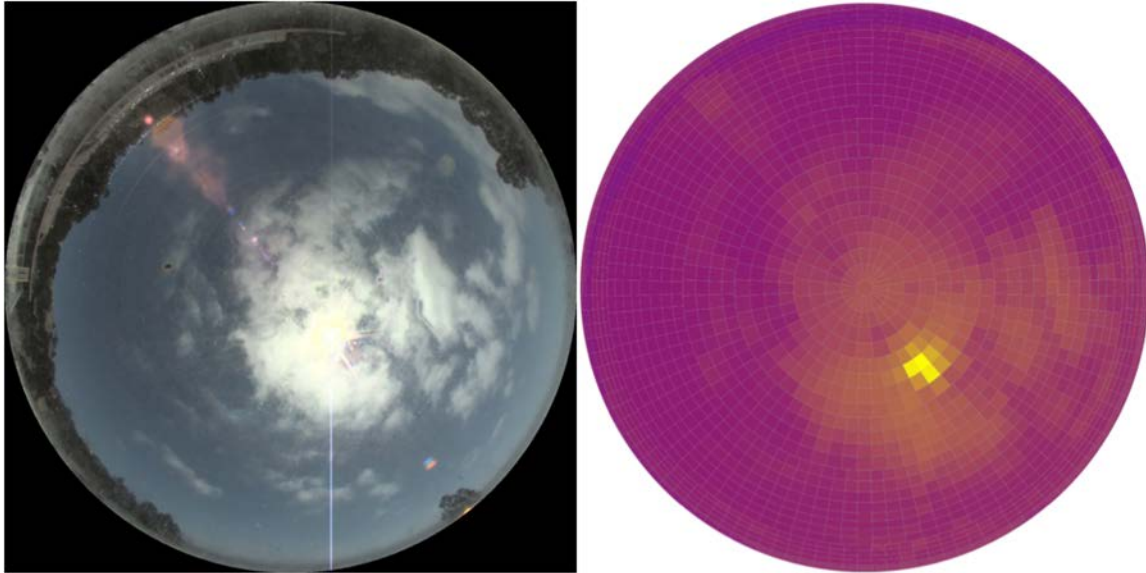


Figure 5. Luminance data from the HDR image of the sky dome (left) was mapped to the Tregenza hemispherical basis subdivided by a factor of 4 (right).

3.2.2. Generation of the F matrix: Subdivision of the window

Similar to the three-phase method, computing the illuminance or luminance contribution from a subdivided window can yield more accurate results than modeling the whole window, particularly if the incident sunlight is not distributed uniformly across the window surface. This is exemplified in the case of a window with an awning where direct sunlight hits the lower unshaded portion of the window, whereas the upper portion is shaded. Without subdivision, incident flux on the window plane is averaged over the entire window surface (since the flux is represented by a single F matrix). With a subdivided window, incident average energy over small areas is likely to be closer in value to the actual incident energy (Figure 6).

Initial simulations demonstrated that the illuminance levels did not track measured data well under clear sky conditions for the non-subdivided window. The simulations significantly overestimated workplane illuminance near the window. The window was subsequently subdivided into an upper and lower section at the height of the workplane illuminance sensors to better map incoming flux to what the sensors actually “see”. F apertures and F matrices were computed for each of these areas of the window. With $F1$ and $F1H$, there were two resultant F matrices for the window. With FN , there were a total of seven F matrices (the top horizontal F aperture was not subdivided). After this subdivision, errors between the simulated and measured data under clear sky conditions were significantly decreased. An example comparison on a clear sunny day is given in Figure 7. Results for the subdivided window are given in Section 4.

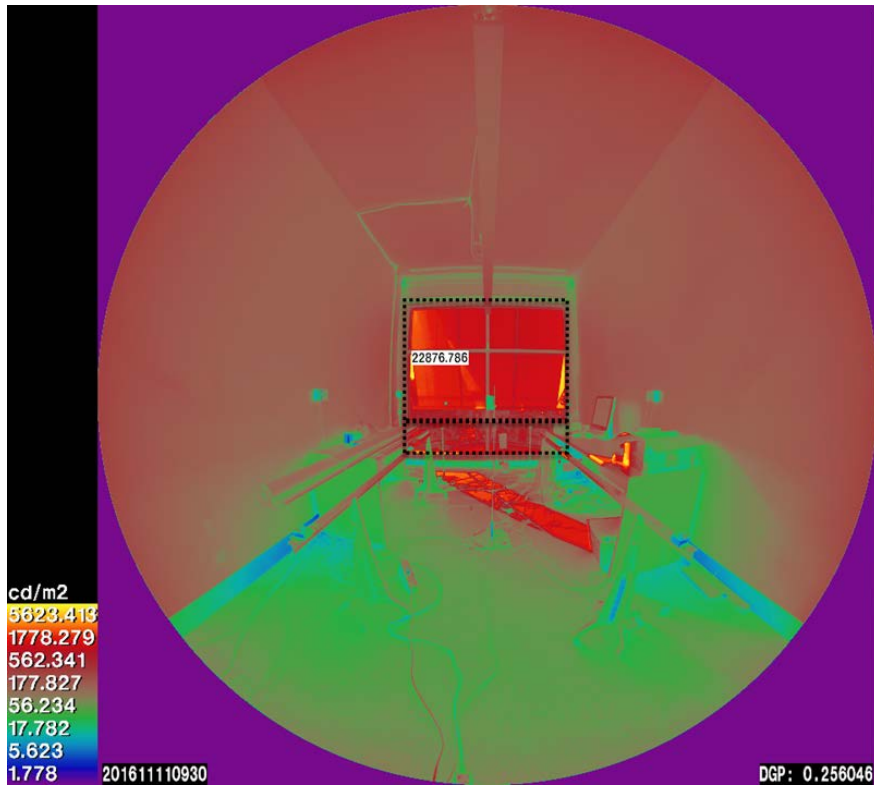


Figure 6. Falsecolor HDR image depicting the measured luminance of surfaces within the test room (January 11, 9:30 AM ST). The image was captured by an HDR camera in the full-scale test chamber with its view looking from the back of the room towards the window with the awning at the 125° winter position. Note the sunlight patch on the floor near the window. The window subdivision is depicted as an overlay to this image, where incident sunlight on the upper and lower areas is averaged in the simulations over these respective areas.

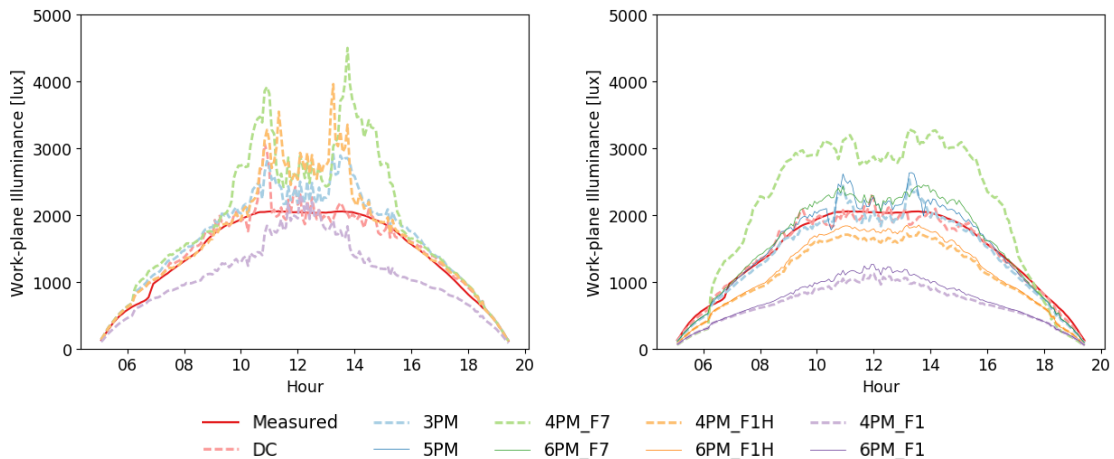


Figure 7. Workplane illuminance near the window on a sunny day (July 14, 2016) where the window was modeled as a single area (left), or sub-divided into two areas at the workplane sensor height (right). Awning angle: 50°.

3.2.3. Generation of the F matrix: Hemispherical basis resolution

For the four-phase method (and to a lesser degree for the six-phase method), accuracy is also affected by the hemispherical basis resolution of the V matrix. In both Equations 4-6, note how the resolution of the V matrix is coupled to the resolution of the T matrix. The resolution of the T matrix however is constrained by the maximum *uniform*⁵ hemispherical basis resolution produced by BSDF generation tools like *genBSDF*⁶. The highest BSDF resolution that can be generated using *genBSDF* is the Klems 145x145 basis, for example.

This is relevant in the case of the FN aperture approach for this particular awning configuration. As seen in Figure 7 above, the F7 simulated data were significantly greater than the measured workplane illuminance even after the window subdivision. The east and west FN apertures were computed with the Klems 145x145 basis, so flux from grazing angles were transferred through 12 large-area patches and resulted in a broad distribution of this flux within the room. If the Tregenza hemispherical basis is used for the F matrices, flux from grazing angles is transferred through 30 patches (compared to 12) and is distributed over a much smaller area within the room, improving accuracy (Figures 8-9). The Tregenza sky has more than double the resolution at grazing angles than the Klems basis.

There were no coplanar indoor shades installed at the window in the test chamber, so there was no need to represent the window with a BSDF T matrix in the simulations. Therefore, the resolution of all matrices could be increased to better isolate sources of error. The window was therefore modeled as a glass material with a refractive index of 1.52 and included in the computation of the view V matrix. The T matrix was removed from the matrix calculation (or it could have remained in the equation and have been represented by elements with the value of 1). For the F matrices, we used the Tregenza hemispherical basis subdivided by a multiplication factor of two (Reinhart MF:2 or 577x577).

Note that for the five- and six-phase methods, the C matrices were computed using the Klems basis instead of the tensor tree basis for the awning fabric. This is because the fabric exhibited Lambertian diffusion, so high resolution tensor tree BSDF data were not required. The projecting geometry of the awning was modeled with its true geometry (i.e., sharp-edged shadows on room surfaces), but sunlight passing through the awning fabric was modeled at low resolution using Klems BSDF data.

The Radiance ray-tracing simulation parameters are given in Table 2 and basis resolution of all matrices used for the simulation results in Section 4 are summarized in Table 3.

⁵ As opposed to the variable resolution, tensor tree basis.

⁶ Descriptions of the *genBSDF* tool can be found in the Radiance manual repository at: <https://radiance-online.org/learning/documentation/manual-pages> and the tutorial https://radiance-online.org/learning/tutorials/Tutorial-genBSDF_v1.0.1.pdf, accessed January 10, 2018. The resolution of the BSDF can be increased through a simple modification to the *genBSDF* code but this increase in resolution will also increase computation time.

Table 2

Radiance simulation parameters for matrix calculations.

	V (V image)	F	D or D'	C _{R-ds}	C _{F-ds}	V* (V* image)
ambient bounces (-ab)	12 (8)	4	4	1	3	12
ambient divisions (-ad)	60,000 (30,000)	10000	10000	1024	1024	200,000 (20,000)
limit weight (-lw)	1.00E-05 (5.00E-04)	1.00E-04	1.00E-04	1.00E-03	1.00E-03	1.00E-06 (5.00E-05)
ray count (-c)	0 (9)	5000	5000	1	1	1

Note: V* is the view matrix used in the two-phase DC method, where rays are traced from a point in the room to the sky instead of the window.

Table 3Resolution of the Tregenza hemispherical bases⁷ used for the matrix calculations.

	Sky component				Sun component	
	V	F1, F1H, FN	D or D'	S, S _d	C _{ds} , C _{R-ds} , C _{F-ds}	S _{sun}
2-phase method (DC)	s x 2306			2306 x n		
3-phase method (3PM)	s x 577		577 x 2306	2306 x n		
4-phase method (4PM)	s x 577	577 x 577	577 x 2306	2306 x n		
5-phase method (5PM)	s x 577		577 x 2306	2306 x n	s x 5186	5186 x n
6-phase method (6PM)	s x 577	577 x 577	577 x 2306	2306 x n	s x 5186	5186 x n

Notes:

- All matrices (V, F, D, S, S_d) were defined with the Tregenza, not the Klems hemispherical basis.
- Two sets of matrices defined for the subdivided window.
- There was no operable coplanar shading at the window so the window glass material was included in the computation of the V matrix. Therefore, the T matrix is not given in the table.
- For the F and C matrices, the NCS was represented by geometry and BSDF material type (Klems 145x145 resolution).
- n = number of time steps and corresponding sky condition; n' = number of sun positions in the Northern and Southern Hemispheres (Figure 1) plus the ground patch.
- s = number of sensor points in the interior space.
- For S_{sun}, the modeled sun locations could be reduced to those for a specific latitude and window orientation in order to substantially reduce matrix computation time.

⁷ The Reinhart subdivision of the Tregenza hemispherical basis is described by multiplication factors (MF), resulting in the following number of patches (the center patch is not subdivided) – MF:2 = 145*2² = 577 patches; MF:4 = 145*4² = 2305 patches; MF:6 = 145*6² = 5185 patches.

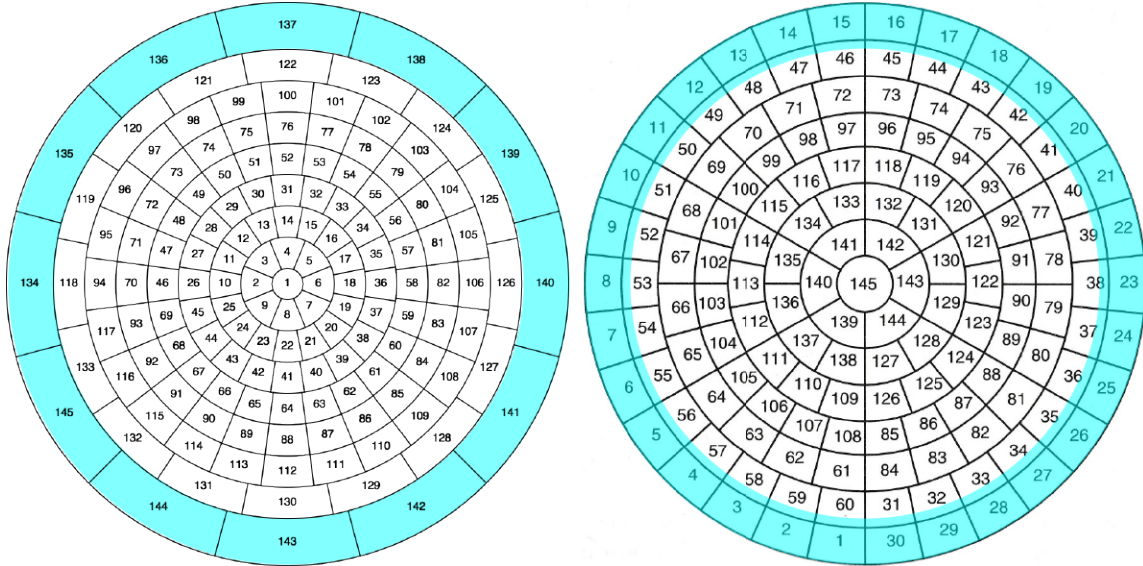


Figure 8. Images showing the subdivision scheme for the Klems (left) and Tregenza (right) hemispherical bases. The patches associated with grazing angles are shaded in blue.

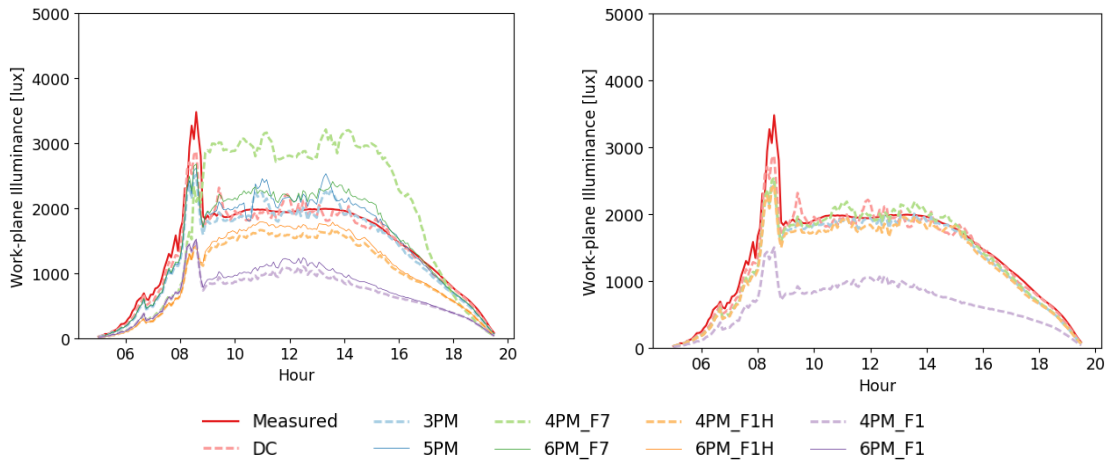


Figure 9. Workplane illuminance on a sunny day (July 12, 2016) with the subdivided window, where the Klems basis (left) or the Tregenza/Reinhart MF:2 basis (right) was used for the F7 matrix. The F7 matrix simulation is shown with the green lines and the measured data are shown with the solid red line. Awning angle: 50°.

3.2.4. Generation of the F matrix: Placement of the F aperture relative to the facade

In this study, the NCS is an operable awning that can be extended and retracted, varying the distance between the outer edge of the awning and the facade. In order to encompass all possible positions of the awning, the F1 aperture was placed at a distance where the awning's outer edge was most extended away from the facade. This aperture placement left a large gap between the F1 aperture and the facade, resulting in loss of total flux between the window and the F1 aperture as described in Section 2.3. When there is a large gap, the F1 aperture only receives rays from part of the hemispherical directions. Essentially, rays leaving the window surface at near grazing angles are not received by the F1 aperture. Consequently, in the modified daylight (D') matrix, rays sent by the F1 aperture at near grazing angles are translated to zeros

when passing to the facade (F) matrix. Simply put, a F1 aperture placed far from the facade will omit rays coming through the top and sides of the F1 aperture. This definition of the F1 aperture should serve as a demonstration of a worst case scenario and the consequence of leaving a large gap between the F1 aperture and the facade.

3.2.5. Luminance and discomfort glare

Simulated renderings were generated at a position that matched that of the HDR camera in the rear of the room (Figure 10). The rendering parameters and matrix resolution are given in Tables 2-3. For all methods, the Klems basis was used to model the roller shade fabric since the BSDF exhibited Lambertian properties (i.e., no specular transmission of direct sunlight through the fabric).

Total luminance levels were extracted from each image for sample areas on the ceiling, wall and floor (approximately 450 pixel area) shown in Figure 10. The daylight glare probability (DGP) index was also computed from the measured and simulated images using the software tool *evalglare* with default settings. Potential glare sources were identified by pixel luminances levels that were five times the average image luminance. The electric lighting was turned off in the outdoor testbed to minimize potential confounding errors with the simulations.

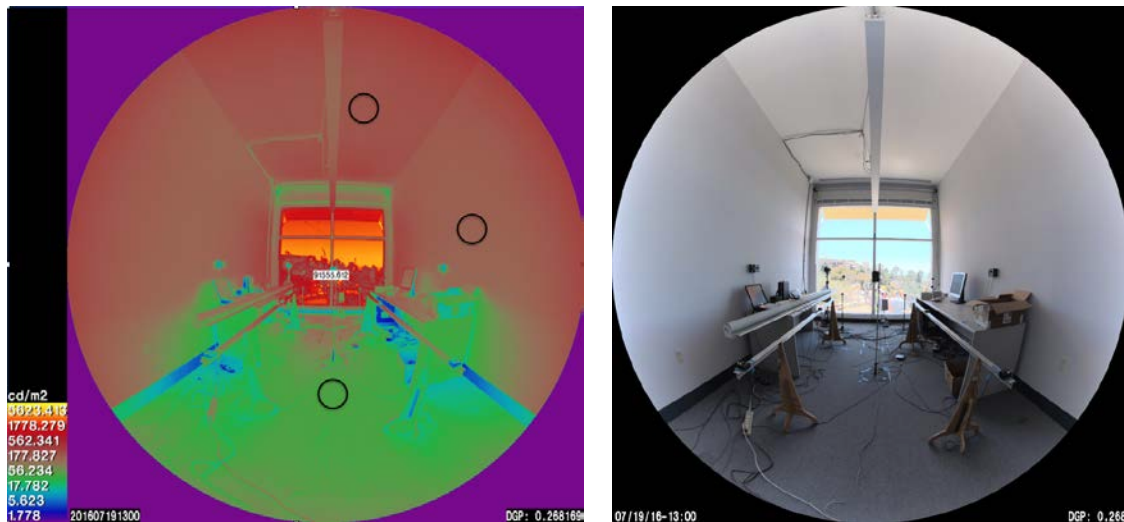


Figure 10. Locations on the wall, ceiling, and floor where luminance data were measured and simulated. This was also the field of view used for the calculation of discomfort glare.

4. Results

4.1. Workplane illuminance: Comparison with field measured data

Comparisons between field measured data from the Advanced Windows Testbed and simulated workplane illuminance data are given for a clear summer day in Figure 11. The simulated data were produced using the various matrix-based algebraic methods described in Section 2. The awning was extended to just avoid direct sunlight on the workplane illuminance sensors nearest the window. Simulated workplane illuminance levels at the six locations tracked measured values well over the course of the day.

Simulations for sensor locations nearest the window performed the worst relative to sensors further from the window because they were more sensitive to spatial averaging produced by the matrix approach. The four- and six-phase methods with the F1 aperture performed the worst as expected due to loss of total flux transfer in the F1 and D' matrices, as described in Sections 2.3 and 3.2.4. Among the remaining seven matrix-based methods, there was no obvious winner in this set of simulations.

On a clear winter day, simulations were carried out with relatively low sun angles. The awning was extended nearly all the way down and obstructed most of the view, however sunlight was still admitted through the sides of the awning in the morning and afternoon hours. Errors due to spatial averaging from the matrix approach were more significant with low sun angles, especially for locations near the window, as shown in Figure 12. Whereas the three- and four-phase methods performed poorly, the five and six-phase methods excelled, predicting workplane illuminance levels more accurately by separating calculation of the diffuse sky contribution from the direct sun contribution.

The following scatter plots (Figure 13) show the level of agreement between the field measurements and simulation results for one of the workplane illuminance sensors nearest the window. Data are given for all measurement periods (5-min interval data, all daylight hours during the summer, 8:00 AM-6:00 PM ST during the winter) and all nine simulation methods. The workplane illuminance nearest the windows were the most challenging to predict. Overestimation of workplane illuminance (centered around the 2000 lux illuminance level for the measured condition, as illustrated by the winter plots), occurred for all but a few of the methods: i.e., five-phase and the six-phase method with the F1H aperture. This overestimated simulated data were likely caused by the direct sun contribution being represented by a large solid angle. This overestimation was most significant with the three- and four-phase methods, then decreased with the five- and six-phase methods, which provided a more accurate representation of the solar disc. In the case of the six-phase method with the F7 aperture, overestimation still occurred with the Tregenza basis (MF:2). Additional increased resolution would likely improve accuracy.

In general, the results showed that simulated workplane illuminance values using all methods except for the four- and six-phase methods with the F1 aperture (i.e., 4PM_F1, 6PM_F1) were valid compared to the measured illuminance values (Tables 4-5). For middle to rear sensors, the normalized mean absolute error between measured and simulated results for the summer and winter periods range was 6.7-15.8%. For the sensors nearest the window, the error range was 10.3-23.6%. Errors for all sensors and all test periods are summarized in Table 6 and Figure 14. The differences between valid methods were negligible in this study.

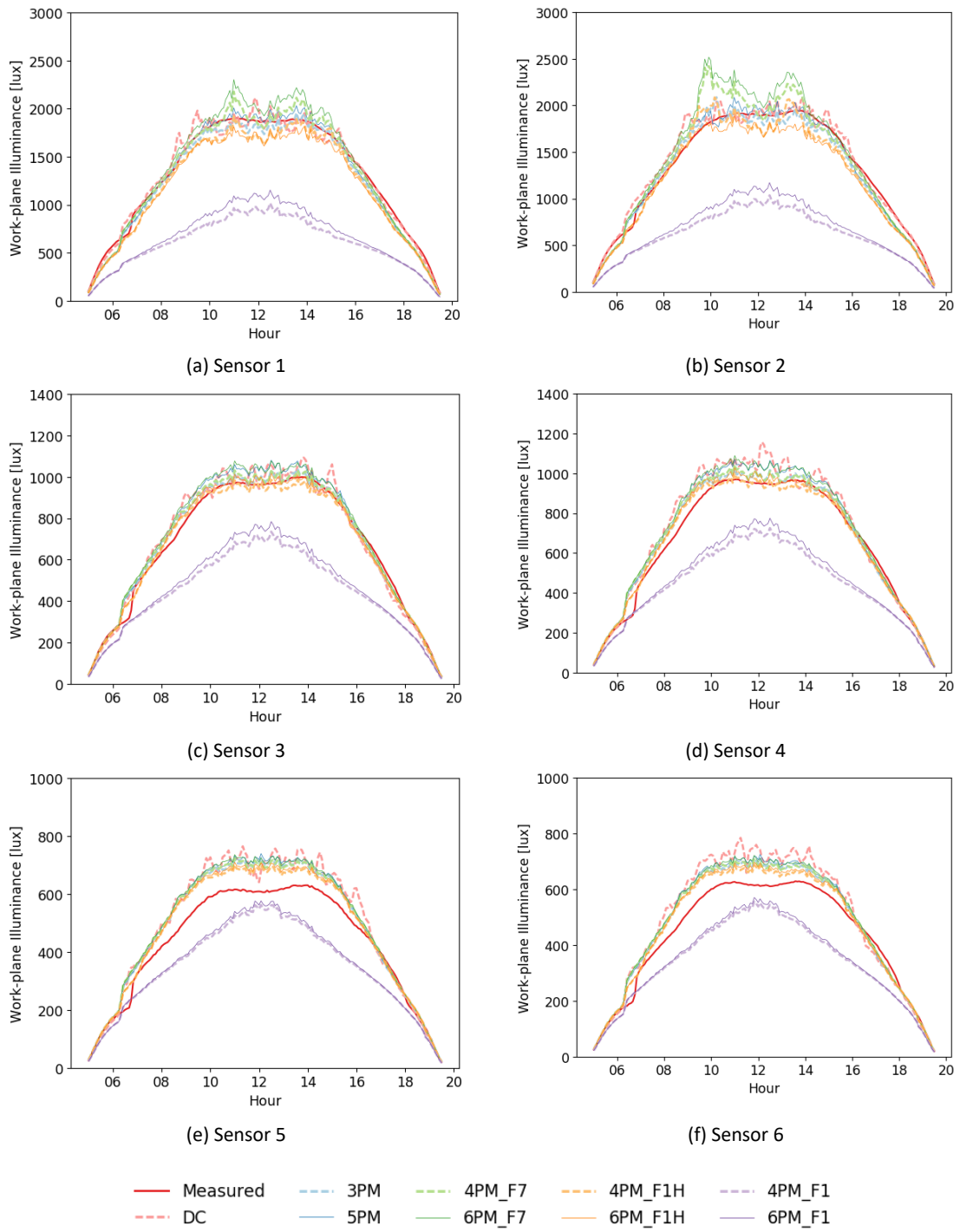


Figure 11. Measured and simulated workplane illuminance at all six sensor locations on a clear summer day (July 10, 2016). Sensors 1-2 were nearest the window.

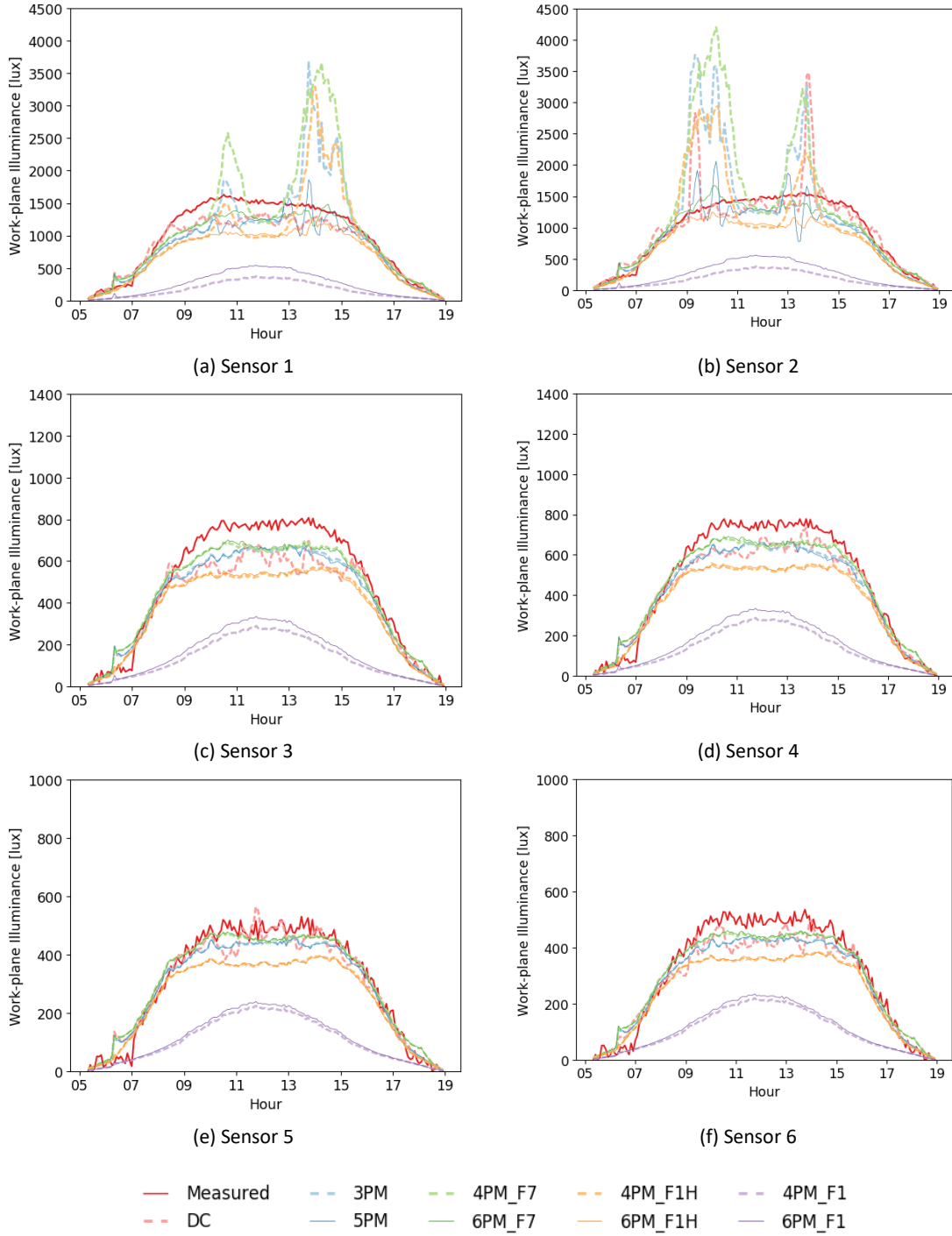


Figure 12. Measured and simulated workplane illuminance at all six sensor locations on a clear winter day (April 30, 2017). Sensors 1-2 were nearest the window.

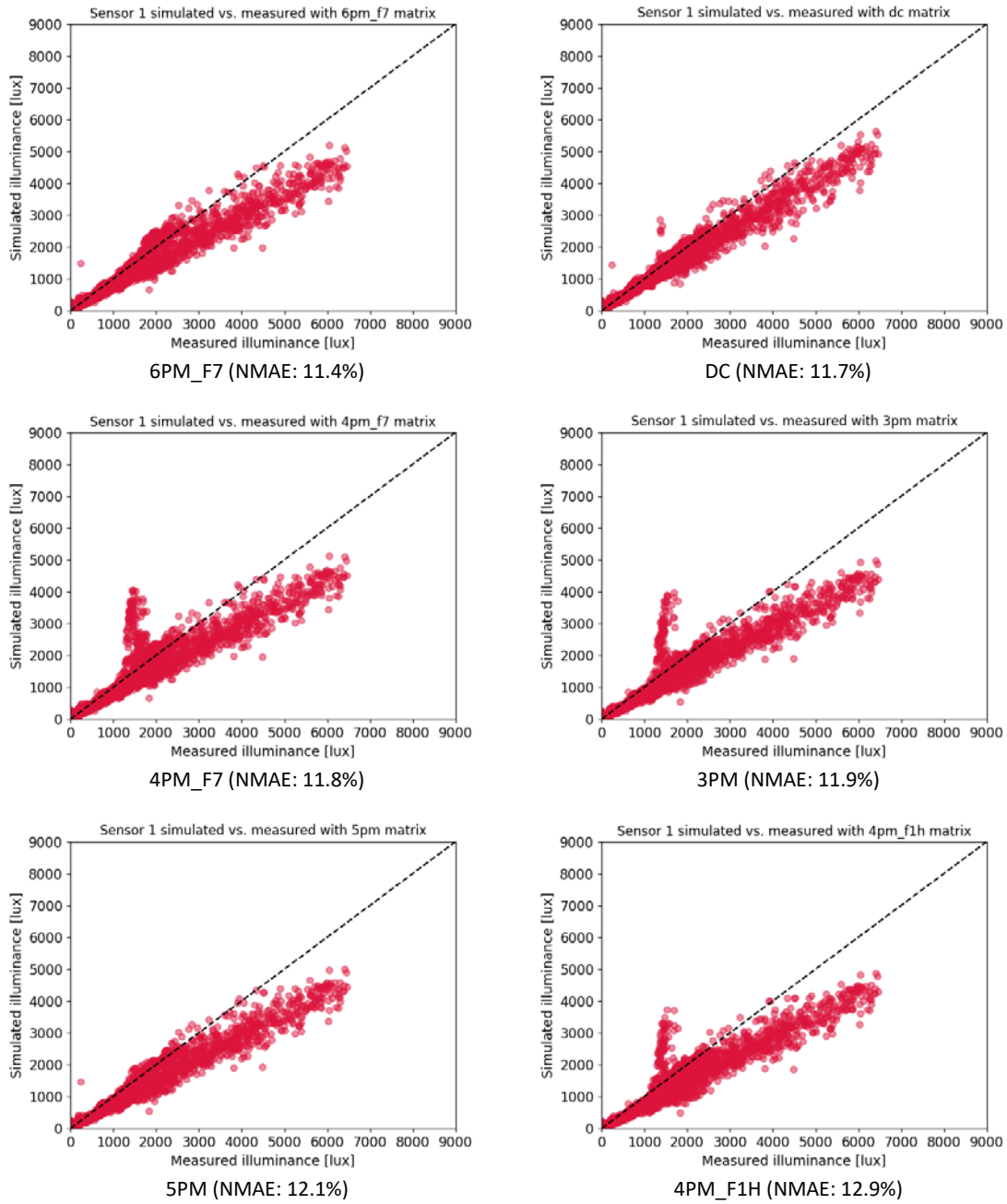


Figure 13. Scatter plots showing measured (x-axis) and simulated (y-axis) workplane illuminance at sensor #1 (near the window) for the entire monitored period using different matrix-based simulation methods. Agreement is best for the top row of graphs (DC and 6PM_F7) and progressively worse for methods below these graphs.

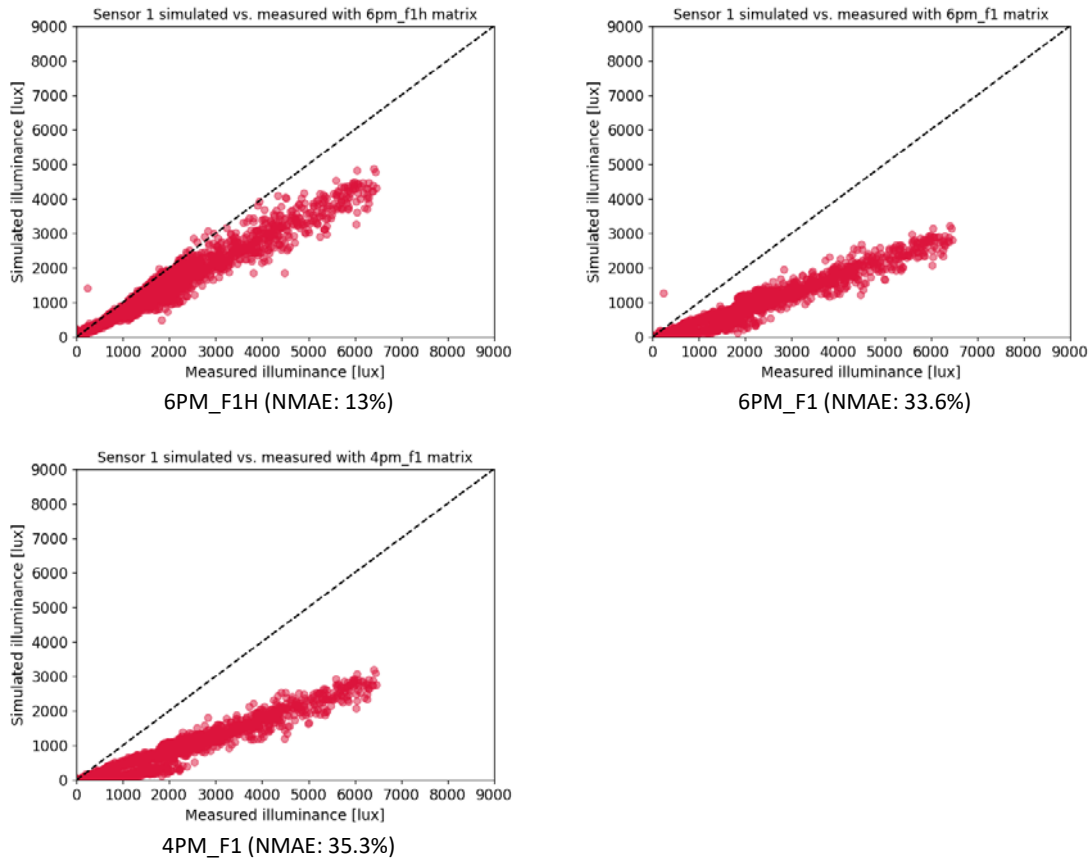


Figure 13 (continued). Correlation between measured (x-axis) and simulated (y-axis) workplane illuminance at sensor #1 (near the window) for the entire monitored period for different matrix-based simulation methods. Agreement is best for the top row of graphs (DC and 6PM_F7) and progressively worse for methods below these graphs.

Table 4

Normalized mean absolute error between measured and simulated workplane illuminance; summer, awning angle 50°.

Sensor distance from window	Front sensors	Middle sensors	Rear sensors
	0.76 m	2.28 m	3.80 m
	2.49 ft	7.48 ft	12.46 ft
Matrix approach:			
DC	15.9%	10.4%	13.3%
3PM	21.7%	7.0%	9.6%
5PM	21.6%	8.3%	10.3%
4PM_F1	57.4%	30.4%	23.6%
4PM_F1H	23.5%	6.7%	8.1%
4PM_F7	21.8%	7.1%	9.5%
6PM_F1	55.0%	28.2%	22.7%
6PM_F1H	23.6%	6.7%	8.6%
6PM_F7	22.4%	8.5%	10.3%

Table 5

Normalized mean absolute error between measured and simulated workplane illuminance; winter and spring, awning angle 125°.

Sensor distance from window	Front sensors	Middle sensors	Rear sensors
	0.76 m	2.28 m	3.80 m
	2.49 ft	7.48 ft	12.46 ft
Matrix approach:			
DC	10.3%	10.1%	8.1%
3PM	18.4%	10.0%	8.2%
5PM	14.1%	10.1%	8.1%
4PM_F1	42.8%	36.9%	33.4%
4PM_F1H	20.7%	15.6%	13.9%
4PM_F7	19.0%	7.8%	6.9%
6PM_F1	40.6%	35.0%	32.3%
6PM_F1H	19.1%	15.8%	13.8%
6PM_F7	10.9%	7.8%	6.8%

Table 6

Normalized mean absolute error between measured and simulated workplane illuminance; all sensors, all test periods.

Matrix approach:	All data
DC	11.7%
3PM	11.9%
5PM	12.1%
4PM_F1	35.3%
4PM_F1H	12.9%
4PM_F7	11.8%
6PM_F1	33.6%
6PM_F1H	13.0%
6PM_F7	11.4%

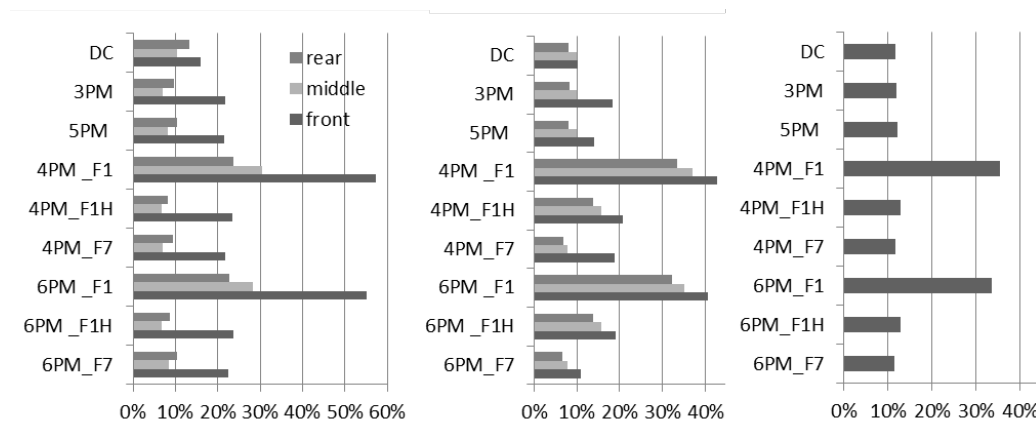


Figure 14. Normalized mean absolute error (NMAE) between measured and simulated workplane illuminance at the rear, middle, and front (nearest the window) of the room. Left: Summer, awning angle 50°. Middle: winter and spring, awning angle 125°. Right: All sensors, summer and winter test periods.

4.2. Luminance and DGP data: Comparison with field measured data

For the summer period, there was no direct sun on the sampled areas of the ceiling, wall, and floor and there was little to no sunlight that entered deep into the space due to the obstruction by the awning. Under these diffuse daylight conditions, simulated luminance levels for the wall and ceiling tracked measured levels to within 5-7%, excluding the four-phase method with F1 aperture (4PM_F1), while for the floor, errors were slightly greater (4-12%), which was likely due to inaccurate modeling of the carpet and possible shadowing from the nearby instrumentation support rails, although this effect is likely to be small (Figure 15 left column; Table 7).

For the winter period (Figure 15, right column), the situation was more challenging due to low angle sun that entered the space. The range of error was 14-32% for the sampled area on the ceiling and 30-45% for the wall and floor, excluding the four- and six-phase methods with F1 aperture (4PM_F1 and 6PM_F1). Sunlight is the probable cause for the higher levels of error on the wall and floor. Ranking methods by level of error for the wall sampled area, the four- and six-phase methods with the F7 aperture yielded the lowest error (36%), the dc, three-, and five-phase methods without the F matrix yielded slightly higher levels of error (39-40%), and four- and six-phase methods with the F1H yielded the greatest error (44-45%). Interestingly, there was no significant difference in error between the methods with and without the direct sun component directly modeled (e.g., four- versus six-phase methods). This was likely because the sampled areas were not exposed to unobstructed direct sunlight and transmitted sunlight through the awning was diffused by the Lambertian properties of the fabric. Overall, however, the range of normalized mean absolute error for the summer and winter periods and three sampled areas in the room was between 14.8-17.5%.

Simulated values for the daylight glare probability (DGP) index agreed well with measured values (6.4-8.6% error) with the exception of the four- and six-phase methods with the F1 aperture (12.0-15.2% error; Figure 16-17 and Tables 7-8). The larger error for the four- and six-phase methods with F1 aperture can be explained by unaccounted flux in the F1 matrix.

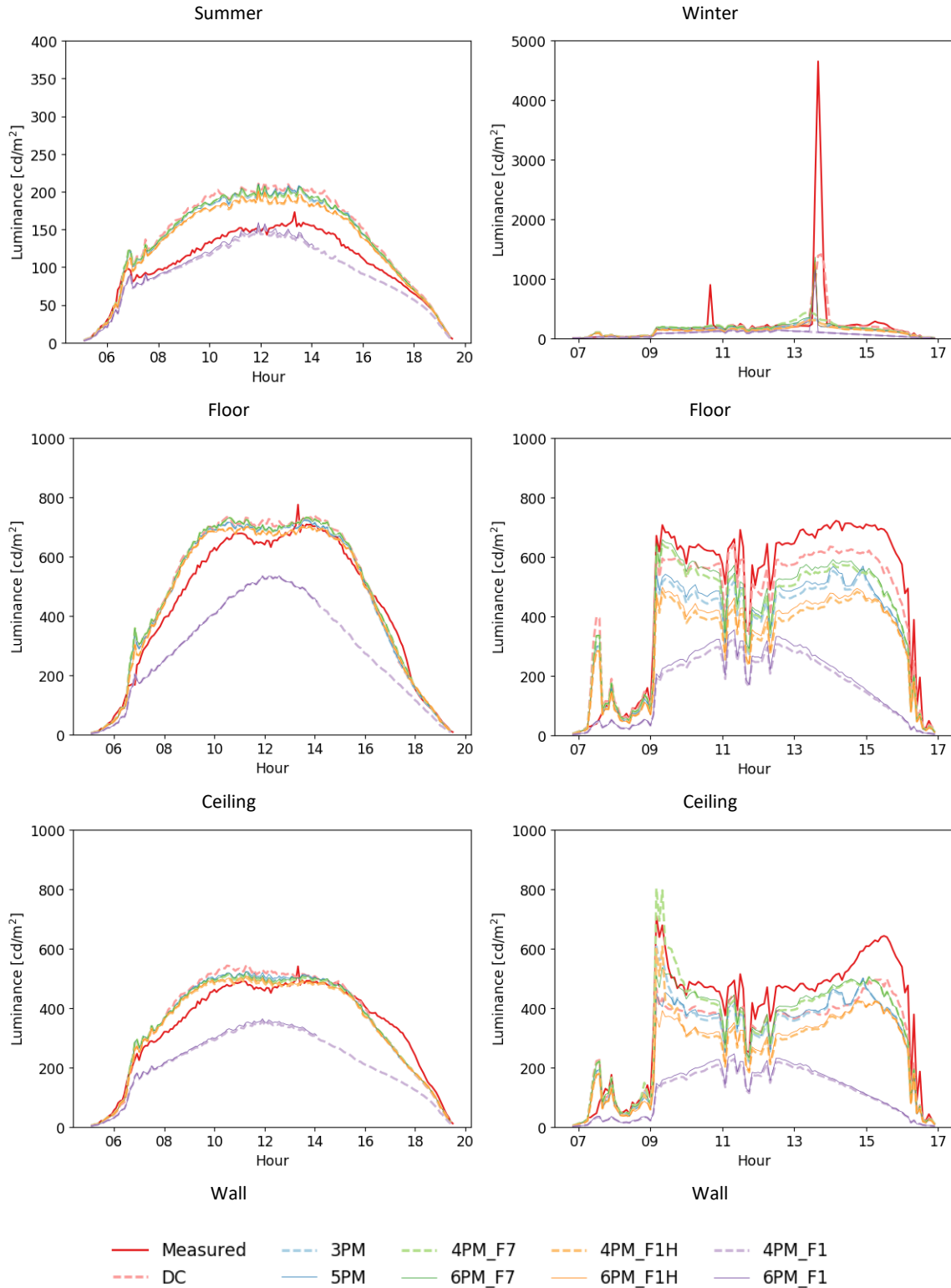


Figure 15. Simulated versus measured luminance values on the floor (top graphs), ceiling (middle), and wall (lower) for two awning position during summer (left column, July 20) and winter (right, November 12).

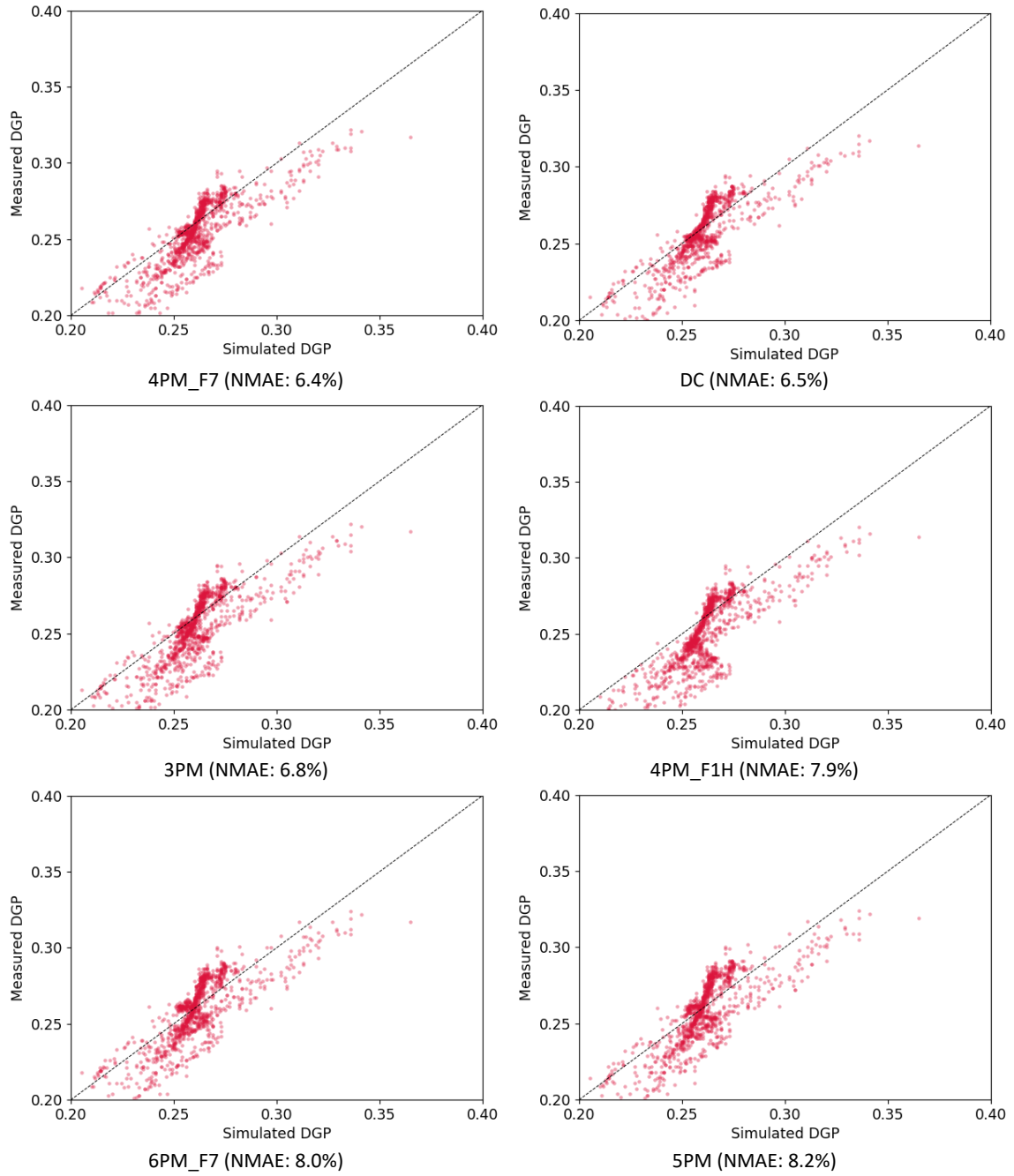


Figure 16. Scatter plots between measured and simulated DGP for all simulation methods. Agreement is best for the top row of graphs (3PM and 5PM) and progressively worse for methods below these graphs.

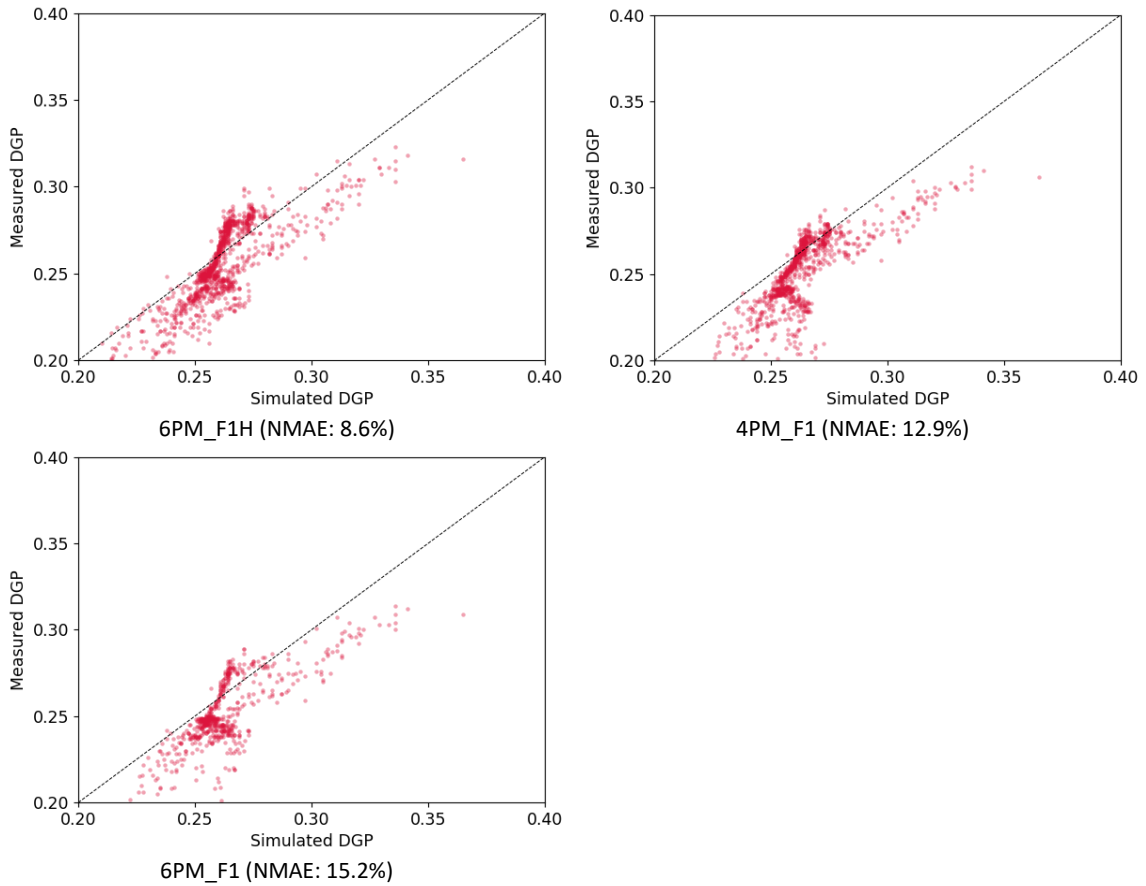


Figure 16 (continued). Correlation between measured and simulated DGP for all simulation methods. Agreement is best for the top row of graphs (3PM and 5PM) and progressively worse for methods below these graphs.

Table 7

Normalized mean absolute error between measured and simulated luminance; three locations in the room, two awning angles (summer 50°, winter 125°).

Surface	Floor		Wall		Ceiling		All
	50°	125°	50°	125°	50°	125°	
<i>Matrix method:</i>							
DC	11.7%	30.1%	6.2%	39.0%	6.0%	14.2%	14.8%
3PM	9.5%	40.2%	4.8%	39.3%	4.8%	25.8%	16.1%
5PM	9.6%	39.0%	5.0%	39.6%	4.8%	24.1%	15.9%
4PM_F1	8.0%	58.1%	19.3%	66.0%	17.9%	55.5%	30.1%
4PM_F1H	9.5%	43.3%	4.7%	43.6%	4.8%	32.3%	17.5%
4PM_F7	11.2%	42.2%	5.1%	36.2%	5.7%	20.0%	16.1%
6PM_F1	3.7%	55.9%	7.0%	63.2%	6.4%	53.7%	22.9%
6PM_F1H	9.7%	42.2%	4.8%	44.8%	4.8%	30.5%	17.4%
6PM_F7	11.3%	39.9%	5.3%	35.5%	5.7%	18.3%	15.7%

Table 8

Normalized mean absolute error between measured and simulated daylight glare probability (DGP).

Matrix method	Overall error
DC	6.5%
3PM	6.8%
5PM	8.2%
4PM_F1	12.9%
4PM_F1H	7.9%
4PM_F7	6.4%
6PM_F1	15.2%
6PM_F1H	8.6%
6PM_F7	8.0%

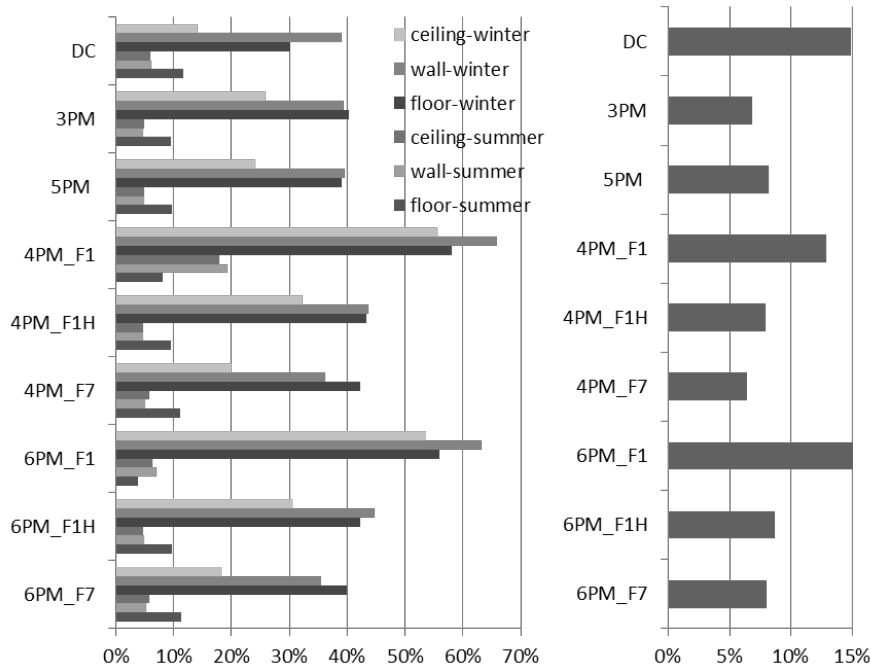


Figure 17. Left: Normalized mean absolute error between measured and simulated luminance; three locations in the room (ceiling, wall, and floor), and two awning angles (summer 50°, winter 125°). Right: Normalized mean absolute error between measured and simulated daylight glare probability (DGP).

4. Discussion

Comparisons made between simulated and measured data indicate that the four- and six-phase methods yielded reasonable results with trends that could be explained by the modeling approach. Accuracy was improved when the F aperture was constructed to account for the majority of incident flux on the window plane (i.e., F1H and FN apertures). Subdivision of the window and use of the Tregenza versus the Klems basis for the F matrices yielded greater accuracy in the spatial distribution of flux within the room. Increased resolution of the F, T, and V matrices also improved spatial accuracy. Finally, the direct sun

Table 9
Matrix dimension with and without T matrix.

Matrix	Dimension without T matrix	Dimension with T matrix
V	$s \times 577$	$s \times 145$
T	none	145×145
F	577×577	145×577
D'	577×2306	577×2306
S	$2306 \times n$	$2306 \times n$

Notes:

n = number of time steps and corresponding sky condition.

s = number of sensor points in the interior space.

contribution to workplane illuminance was modeled more accurately when the solar disc was modeled separately using the correct apex angle with the six-phase method. Errors presented in Tables 4-8 represent modeling approaches where the above strategies were applied to improve accuracy. Systematic errors due to discrepancies between the model and the real-world space and surroundings are included in the total error estimates. The ranking of methods from best to worst accuracy assume use of the same basis resolution between all modeling approaches.

Use of the higher resolution BSDF for the T matrix in order to identify sources of error with the four- and six-phase methods was useful for the validation task but for practical applications, this approach is somewhat problematic. Assuming that most applications involve operable coplanar indoor shades, the T matrix, omitted for the validation, will be needed for simulations. However, Radiance *genBSDF* and LBNL WINDOW tools currently produce BSDF data using the uniform Klems basis, not the Tregenza basis with high resolution. The *genBSDF* tool could be modified to produce high resolution BSDFs (using either the Klems or Tregenza basis definition). Doing the same for the WINDOW software may be a more involved process. To evaluate the benefit of using this capability, end users are advised to perform a comparative analysis between the DC method and four- or six-phase methods for their application to determine whether the selected method is sufficient. Table 9 shows the dimensions of each matrix with and without the Klems 145x145 limit of the T matrix. Notice that in the scenario without the T matrix, the sampling resolution of the V, F, and D' matrices can be set to higher resolutions.

When it comes to applications, the four- and six-phase methods can reduce overall modeling and computation time for cases where the geometry and/or material properties of the non-coplanar shading element are being parameterized. A simple use case would be development of design guidance for selecting the best fabric for an awning based on adequate daylight admission and glare control for a variety of contexts (e.g., different window orientations, urban versus unobstructed site). The BSDF of "k" types of fabric would be used to generate "k" sets of F and C matrices. The F and C matrices would then be a parameter in the matrix calculation with the remaining V, T, D', and S matrices computed once in the initial set up. The amount of time saved for 100 fabric permutations compared to the two-, three-, and five-phase methods would be significant.

The comparison of simulated to measured data demonstrated that the intensity and distribution of transmitted solar radiation through the NCS-shaded window was correct, therefore room surface heat gains due to transmitted solar radiation will also be correct. Incident solar radiation on the exterior surface of the window was also modeled correctly, therefore modeled window heat gains due to absorbed solar radiation will also be correct. For the thermal portion of the solar heat gain calculation, this validation study does not

Table 10
Matrix formulation for parametric modeling.

	Parameters	Example
V*S	No parametric modeling	No parameterization
VDS	Interior and exterior parameters	Interior parameter: room reflectance; exterior parameter: reflectance of adjacent building wing
VFDS	Interior, NCS, and exterior parameters	NCS parameter: non-coplanar awning angle and fabric; interior and exterior reflectance
VTDS	Interior, CPS, and exterior parameters	CPS parameter: coplanar indoor or outdoor venetian blind angle; interior and exterior reflectance
VTFDS	Interior, CPS, NCPS, and exterior parameters	All parameters; awning angle, indoor venetian blind angle; interior and exterior material reflectance

Note : V* is the view matrix used in the two-phase DC method, where rays are traced from a point in the room to the sky instead of to the window.

make claims regarding improved accuracy. Models involving the conductive, radiative, and convective heat flow in and around NCS geometries were not investigated. If the window has low-emittance properties and the NCS is not designed with thermal bridging between the indoors and outdoors, then these other effects are estimated to be small. In EnergyPlus, for example, opaque, rectilinear NCS are modeled using a simple shadow calculation; no additional modifications to the window thermal heat flow calculations were implemented.

Constructing the F apertures then computing F matrices can be a barrier to the adoption of this method in software tools. First, the user has to decide which type of F aperture should be defined for their application. If the non-coplanar shading (NCS) element has a shallow depth from the outer edge of the NCS to the face of the facade, the F1 aperture may be sufficient (due to limited daylight contributing to the scene from behind the façade) and is relatively quick to model. The F1H aperture requires more work to set up while the FN aperture is the most time-consuming to set up and compute but provides the most accurate results. If the goal of the end user is to conduct a parametric study where the surroundings, building orientation, and NCS objects are subject to change, it is likely worth the effort to use the four- or six-phase method. Table 10 lists the various matrix formulations based on which components of the model are being parameterized. If the objective of the study is known, the end user can decide which matrices to construct and combine.

Users also need to consider how to subdivide the window. Subdividing the window into two areas, for example, means there will be two sets of V, T, and F matrices. If there is an operable coplanar shade (e.g., roller shade or venetian blind with variable height positions), then window subdivision is implied in the workflow – the full height of the window will need to be subdivided at each shade height.

To generate the F1H matrix, one can use the Radiance *getbbox* tool to define the F apertures. *Getbbox* calculates the coordinates of the bounding box that encapsulates the window and NCS geometries. These coordinates serve as a guide on how best to place the F1H aperture polygons in the scene. F1H apertures usually consist of four surfaces: top, front, left, and right sides of the NCS. If the window is on the second floor or if the NCS is a significant distance from the facade such that there is light coming from below, a polygon should also be placed at the bottom. Once the polygons are constructed, all polygons are assigned to a single sampler; the polygons' outward facing normals are then averaged based on surface area. Using the normal direction and sampling basis, rays are then traced from the window surface to the F

apertures. For innovative architectural designs, determining what to include in the bounding box can be complicated. For example, NCS elements on an adjacent upper floor may shade the window or an irregular pattern of shading elements may have been designed across the width and height of the façade. The bounding box that maps the flux from the window to the shading device(s) for these cases may span multiple floors and may need to encompass the variations in design (similar to variable depth awnings).

In this validation study, the NCS itself was modeled with the geometry of the awning projection (i.e., overhang with a specified angle) and a BSDF of the fabric material. For an awning fabric with a direct through component (e.g., 1-3% openness factor), the variable-resolution tensor tree basis should be used for the C matrix term, not the uniform Klems basis. For projections made of materials that are modeled with macro-scaled geometry (e.g., expanded metal mesh, perforated metal, louvers), the direct sun contribution can be modeled using proxy geometry and shadow testing within Radiance. The Klems BSDF used to defined the nearly Lambertian fabric was also problematic for the rendering using two-phase method. The error was large using the two-phase method when low specular sampling (-ss 1) was used. Low specular sampling ray was insufficient for integrating the sun and sky component because one specular ray was not enough to sample a large solid angle. The results improved after increasing the specular sampling from 1 to 4000 (RMSE was reduced from 14.8% to 6.5%).

5. Conclusions

Non-coplanar shading (NCS) systems are defined as fixed or operable exterior elements such as overhangs or fins that project out from the face of the façade. These systems can provide significant reductions in solar heat gains but can also diminish daylight availability to the interior. Existing tools enable evaluation of daylight and solar heat gains (e.g., radiosity-based tools and the two-, three- and five-phase matrix-based methods that rely on ray-tracing) but use of parametric analysis to determine the best geometry and materials for the projection can be a slow process. In this study, alternate matrix algebraic methods were developed to facilitate parametric analysis. The four-phase method introduces the F matrix term to the prior validated three-phase method used to model coplanar shading systems. The F matrix models the transfer of flux from the NCS to the surface of the window. Similar to the five-phase method, the six-phase method adds an additional term that separates calculation of the diffuse sky contribution from the direct sun contribution to achieve more accurate spatial resolution of flux within the room interior.

Comparisons with measured data indicate that the four- and six-phase methods yielded simulated results that were within acceptable levels of error. Simulated workplane illuminance agreed with measured data to within 11-13% normalized mean absolute error. Surface luminance agreed to within 16-18%. The daylight glare probability agreed to within 6-9%. The relative ranking of matrix-based methods for determining workplane illuminance were logical. Methods that modeled the direct sun component with the actual size of the sun orb were more accurate than those that depicted the sun with a large solid angle. More detailed approaches to defining the F matrix yielded greater accuracy than simpler approaches.

Results of this model validation of daylighting performance are applicable to solar heat gain performance. Since exterior shading can significantly reduce peak demand, this improved accuracy enables utilities, those involved in demand side management programs, and other stakeholders to more accurately assess the impact of these technologies in supporting grid management and resiliency goals. For applications requiring accurate spatial distribution of solar flux within the room (e.g., evaluation of phase change materials; radiant cooling systems with small-area, local control; thermal comfort modeling using a multi-node physiological model), higher resolution BSDFs may be needed. Field validation of models for computing solar heat gains is planned for future work.

We envision that a likely application of the four- or six-phase methods is the development of prescriptive language advocating use of NCS in building energy efficiency codes and standards. Current standards such as the California Energy Commission Title-24 [40] or the American Society of Heating, Refrigerating and Air-Conditioning Engineers (ASHRAE) 90.1 Standard [41] include a projection factor under the prescriptive approach that relaxes the solar heat gain coefficient (SHGC) requirements if an *opaque* overhang or fin is used. Many architectural projects however specify NCS with angle-dependent transmissive properties (e.g., louvers, slats, fritted glass) in order to improve both solar control and daylighting in buildings. These new models enable parametric modeling for standards development. Other applications mentioned earlier include rating and labeling of commercially available systems, development of new technologies, and development of design guidance for existing commercial shading systems offered by manufacturers.

The current implementation of the models involves use of the command line version of Radiance. A Radiance tutorial with example code has been developed to explain the use of the models and is now available to the public [42]. To facilitate adoption of the NCS models by industry, an additional script has been developed to automatically generate the F1H matrix from a geometric description of the NCS. The script would enable end users to use conventional software tools in a work-around solution or enable software developers to incorporate the new models more easily in their tools.⁸ Incorporation of these models to compute solar heat gains in EnergyPlus is also undergoing development and validation. A BSDF library of exterior shading materials will be needed as input to the simulations.

Acknowledgments

This work was supported by the California Energy Commission through its Electric Program Investment Charge (EPIC) Program on behalf of the citizens of California and by the Assistant Secretary for Energy Efficiency and Renewable Energy, Building Technologies Program of the U.S. Department of Energy under Contract No. DE-AC02-05CH11231. In-kind support was provided by Glen Raven. We would like to thank Dustin Davis, California Energy Commission, and Amir Roth, U.S. Department of Energy, for their continued support for this research.

We would also like to acknowledge the contributions of LBNL team members Jacob Jonsson, Christoph Gehbauer, and Daniel Fuller. Andrew McNeil conceived of the F-matrix approach while at LBNL. He and Christian Humann, Terrestrial Light, provided additional technical support related to their SkyCam. Christopher Meek, Integrated Design Lab, University of Washington, graciously provided us with the geometric model for the UC San Diego project.

References

- [1] D&R International, Ltd., 2011. Buildings Energy Data Book. US Department of Energy, Energy Efficiency and Renewable Energy; Tables 2.1.15 and 3.1.12.
- [2] Huang, J., Hanford, J., and Yang, F., 1999. Residential heating and cooling loads component analysis. Building Technologies Department, Environmental Energy Technologies Division, Lawrence Berkeley National Laboratory, University of California; Figure P-1 and Appendix C: Component Loads Data Tables

⁸ The final version of the script will be released after testing by the Radiance community.

- [3] Huang, J. and Franconi, E., 1999. Commercial heating and cooling loads component analysis, Final Report. Environmental Energy Technologies Division, Lawrence Berkeley National Laboratory, Berkeley, CA.
- [4] Arasteh, D.K., Selkowitz, S.E., Apte, J.S., LaFrance, M., 2006. Zero Energy Windows. In 2006 ACEEE Summer Study on Energy Efficiency in Buildings. Pacific Grove, CA.
- [5] Cho, J, Yoo, C., and Kim, Y., 2014. Viability of exterior shading devices for high-rise residential buildings: Case study for cooling energy saving and economic feasibility analysis. *Energy and Buildings* 82: 771-785.
- [6] Kim, G., Lim, H.S., Lim, T.S., Schaefer, L., and Kim, J.T., 2012. Comparative advantage of an exterior shading device in thermal performance for residential buildings. *Energy and Buildings* 46: 105-111.
- [7] Bülow-Hübe, H., 2000. Office worker preferences of exterior shading devices: a pilot study. In Proc. of the EuroSun 2000 Conference, June, pp. 19-22.
- [8] Van Moeseke, G., Bruyère, I., and De Herde, A., 2007. Impact of control rules on the efficiency of shading devices and free cooling for office buildings. *Building and Environment* 42 (2): 784-793.
- [9] Tzempelikos, A., and Athienitis, A.K., 2007. The impact of shading design and control on building cooling and lighting demand. *Solar Energy* 81(3): 369-382.
- [10] Athienitis, A.K., and Tzempelikos, A., 2002. A methodology for simulation of daylight room illuminance distribution and light dimming for a room with a controlled shading device. *Solar energy* 72(4): 271-281.
- [11] Lee, E.S., Selkowitz, S.E., DiBartolomeo, D.L., Klems, J.H., Clear, R.D., Konis, K., Hitchcock, R., Yazdanian, M., Mitchell, R., Konstantoglou, M., 2009. High Performance Building Facade Solutions. California Energy Commission, PIER, CEC-500-06-041.
- [12] Winkelmann, F. C., 2001. Modeling windows in EnergyPlus. Proceedings of the 2001 IBPSA Building Simulation Conference.
- [13] Loutzenhiser, P.G., Maxwell, G.M., Manz, H., 2007. An empirical validation of the daylighting algorithms and associated interactions in building energy simulation programs using various shading devices and windows. *Energy* 32(10): 1855-1870.
- [14] Bellia, L., De Falco, F., Minichiello, F., 2013. Effects of solar shading devices on energy requirements of standalone office buildings for Italian climates. *Applied Thermal Engineering* 54(1): 190-201.
- [15] Gugliermetti, F., and Bisegna, F., 2006. Daylighting with external shading devices: design and simulation algorithms. *Building and Environment* 41(2): 136-149.
- [16] Saelens, D., Parys, W., Roofthoof, J., De la Torre, A.T., 2013. Assessment of approaches for modeling louver shading devices in building energy simulation programs. *Energy and Buildings* 60: 286-297.
- [17] Sargent, J., Niemasz, J., Reinhart, C.F., 2011. Shaderade: combining Rhinoceros and Energyplus for the design of static exterior shading devices. *Building Simulation*, pp. 1-9.
- [18] Kirmat, A., Koyunbaba, B.K., Chatzikonstantinou, I., Sariyildiz, S., 2016. Review of simulation modeling for shading devices in buildings. *Renewable and Sustainable Energy Reviews* 53: 23-49.
- [19] Tregenza, P.R., Waters, I., 1983. Daylight coefficients. *Lighting Research and Technology*, 15(2): 65-71.
- [20] Mardaljevic, J., 2000. Simulation of annual daylighting profiles for internal illuminance, *Lighting Research and Technology* 32(3): 111-118.
- [21] Reinhart, C.F., Herkel, S., 2000. The simulation of annual daylight illuminance distributions — a state-of-the-art comparison of six RADIANCE-based methods, *Energy and Buildings*, 32: 167–187.
- [22] Reinhart, C.F., Walkenhorst, O., 2001. Validation of dynamic RADIANCE-based daylight simulations for a test office with external blinds. *Energy and Buildings* 33 (7): 683-697.

- [23] Saxena, M., Ward, G., Perry, T., Hescong, L., Higa, R., 2010. Dynamic Radiance – Predicting annual daylighting with variable fenestration optics using BSDFS, Fourth National Conference of IBPSA-USA, New York City, New York, August 11 – 13, 2010.
- [24] Klems, J.H., 1994a. A new method for predicting the solar heat gain of complex fenestration systems: I. Overview and derivation of the matrix layer calculation, *ASHRAE Transactions* 100 (1): 1065-1072.
- [25] Ward, G., Mistrick, R., Lee, E.S., McNeil, A. Jonsson, J., 2011. Simulating the Daylight Performance of Complex Fenestration Systems Using Bidirectional Scattering Distribution Functions within Radiance. *Leukos* 7(4): 241-261.
- [26] McNeil, A. and Lee, E.S., 2013. A validation of the Radiance three-phase simulation method for modelling annual daylight performance of optically complex fenestration systems. *Journal of Building Performance Simulation*, 6(1): 24-37.
- [27] Lee, E.S., Geisler-Moroder, D., Ward, G., 2018. Modeling the direct sun contribution in buildings using matrix algebraic approaches: Methods and validation, *Solar Energy* 160: 380-395.
- [28] AERC, Attachments Energy Rating Council, <http://aercnet.org/>, accessed January 10, 2018.
- [29] ES-SO, 2017. European Solar-Shading Organization, <http://www.es-so.com/>, accessed January 10, 2019.
- [30] Fadzil, S.F.S and Sia, S.J., 2004. Sunlight control and daylight distribution analysis: the KOMTAR case study. *Building and Environment* 39(6): 713-717.
- [31] Ossen, D.R., Ahmad, M.H., Madros, N.H., 2005. Optimum overhang geometry for building energy saving in tropical climates. *Journal of Asian Architecture and Building Engineering*, 4(2): 563-570.
- [32] Caldas, L.G., Norford, L.K., 2003. Genetic Algorithms for Optimization of Building Envelopes and the Design and Control of HVAC Systems. *J. Sol. Energy Eng.* 125(3):343-351.
- [33] Ward Larson, G., Shakespeare, R., 1998. *Rendering with Radiance: The Art and Science of Lighting Visualization*. San Francisco: Morgan Kaufmann.
- [34] Mardaljevic, J., 2000. Daylight simulation: validation, sky models and daylight coefficients. PhD Thesis, De Montfort University, United Kingdom.
- [35] Bourgeois, D., Reinhart, C.F., Ward, G., 2008. Standard daylight coefficient model for dynamic daylighting simulations. *Build. Res. Inf.* 36(1): 68–82.
- [36] McNeil, A., 2013. The Five-Phase Method for Simulating Complex Fenestration with Radiance. <https://facades.lbl.gov/sites/all/files/tutorial-fivephasemethod.pdf> , accessed January 10, 2018.
- [37] J.C. Jonsson, C. Curcija, H.R. Wilson, J. Slack, S. Appert, M. Quinones, S. Zhao, K. Wu and M. Rubin, Measurement Procedure for Optical and Thermophysical Properties of Fenestration Shading Fabrics to be used in WINDOW, 2015, Technical Report, Lawrence Berkeley National Laboratory, Berkeley, CA, October 1, 2015.
- [38] Humann, C., McNeil, A., 2017. Skycam, Terrestrial Light. <http://terrestriallight.com/conc/>, accessed January 10, 2018.
- [39] Wienold J., 2016. evalglare version 2.0. École Polytechnique Fédérale de Lausanne, <https://www.radiance-online.org/community/workshops/2016-padua/presentations/211-Wienold-Evalgaare2.0.pdf>, accessed January 10, 2018.
- [40] California Energy Commission, 2015. 2016 Building Energy Efficiency Standards for Residential and Nonresidential Buildings. CEC-400-2015-037-CMF, California Energy Commission.
- [41] American Society of Heating, Refrigerating and Air-Conditioning Engineers (ASHRAE), 2015. ANSI/ASHRAE/IES Standard 90.1-2016 -- Energy Standard for Buildings Except Low-Rise Residential Buildings. Atlanta: ASHRAE.
- [42] Subramaniam, S., 2017. Daylighting Simulations with Radiance using Matrix-based Methods. <https://radiance-online.org/learning/tutorials/matrix-based-methods>, accessed January 10, 2018.